Standardize Angular Response Function Pre-calculation Requirements for Collimator-Detector Response Modeling in SPECT Imaging

Jie Zhang

A thesis

submitted in partial fulfillment of the

requirements for the degree of

Master of Science

University of Washington

2016

Reading Committee:

Paul E. Kinahan, Chair

Thomas K. Lewellen

Robert S. Miyaoka

Chun Yuan

Program Authorized to Offer Degree:

Bioengineering

University of Washington

Abstract

Standardize Angular Response Function Pre-calculation Requirements for Collimator-Detector Response Modeling in SPECT Imaging

Jie Zhang

Chair of the Supervisory Committee:
Professor Paul E. Kinahan, Ph.D.
Department of Radiology, Bioengineering and Physics

Photon-tracking Monte Carlo simulations of Single Photon Emission Computed Tomography (SPECT) are inherently inefficient. One proposal to speed such simulations is to use Angular Response Functions (ARFs) to model the collimator-detector response. Unfortunately, generation of ARFs is also extremely computation intensive: a table is needed for each incident energy, for each collimator/detector combination, and for each energy window of interest. The method is only useful when the same collimator/detector/energy window combination will be used for a large number of simulations.

In this thesis we report on a systematic way to reduce the number of tables needed, and the number of photons needed to generate a table. We first introduce the background of SPECT imaging system and the Monte Carlo simulation method. We then focus on the generation of ARFs for ^{67}Ga and their implications for quantitative imaging. We incorporated the ARF feature to our public domain emission tomography simulation SimSET and validate the simulation

results by comparing with the experiment results under same configuration. Our method is feasible for a wider range of application.

TABLE OF CONTENTS

LIST OF FIGURES

LIST OF TABLES

ACKNOWLEDGEMENTS

I want to express my deepest gratitude to all the people who have participated in this work and gave me support and help during my graduate studies.

I would like to sincerely thank my mentor, Robert Harrison for his excellent guidance, patience, and humor for the past two and half years to provide me with extraordinary mentorship on my research in the Imaging Research Laboratory (IRL), University of Washington. Robert is a great mentor who teaches me how to be innovative and collaborative in research. I would also like to thank my advisors, Dr. Thomas Lewellen, Dr. Paul Kinahan, and Dr. Robert Miyaoka, for letting me join one of the most outstanding and supportive group in Nuclear Medicine and helping me build a solid understanding of Nuclear Medicine. Also, thanks to my current supervisory committee member, Dr. Chun Yuan, and previous qualifying exam committee members, Dr. James Bassingthwaighte and Dr. Colin Studholme, for teaching me fundamental knowledge in medical imaging and helping me during my research rotations, and qualifying exam.

Moreover, I would like to say thank you to our collaborators, Dr. Eric Frey, Dr. Yong Du, and their group from John Hopkins University for kindly providing the ordered subset expectation maximization (OSEM) software package and helping me throughout my research studies. I would also like to thank Dr. Thomas Carlier from University Hospital of Nantes, France and Dr. Albert Cot from University of Barcelona, Barcelona, for their generous help and patient explanation to my questions related to Angular Response Function (ARF) modeling.

Great thanks to Dr. Hubert Vesselle and Dr. Larry MacDonald for giving me suggestions and important feedback, when I was a novice to the Nuclear Medicine field. Many thanks to other members in our lab, Wendy McDougald, Dr. William Hunter, and Dr. Larry Pierce for their great help and support. I would also like to thank my fellow peers who are or were previously in graduate school Xi Cheng, Chengeng Zeng, Kristen Wangerin, and Tzu-Cheng (Efren) Lee for their help and friendship.

Lastly, I want to thank my parents Chuntao Wang and Aichen Zhang for their unconditional support and love that give me courage and confidence to face and enjoy all the challenges.

Chapter 1. INTRODUCTION

1.1 BACKGROUND AND MOTIVATION

Single Photon Emission Computed Tomography (SPECT) has been a major field in Nuclear Medicine since the 1970's [1]. The availability of the radionuclide ^{99m}Tc and the development of the gamma camera by Anger [2] have led to a rapid development in SPECT imaging technique. SPECT is able to visualize and analyze different organs, tissue functions or properties non-invasively. Therefore, it has many important clinical diagnostic applications in cardiology, oncology and neurology. For example, SPECT is used for studies of myocardial perfusion for assessing coronary artery disease and heart muscle damage following infarction, and cerebral perfusion studies with SPECT also are widespread.

Simulation is an important tool in SPECT imaging research. The true underlying anatomy and physiology is unknown in patient scans, and there are various factors confounding the data: statistical noise, biological variability, patient motion, scattered radiation, dead time, and other data contaminants [3]. The Monte Carlo (MC) method, which is a numerical solution to a problem that models object interacting with other objects or their environment, has been widely used in SPECT simulation.

In SPECT imaging, the collimator-detector response function (CDRF) describes the detected spatial distribution of photons for a given point source position. The CDRF includes the geometric, penetration, septal scatter and x-ray fluorescence components. Blurring and artifacts in the projection images are dependent on the extent to which the CDRF differs from a delta function. Collimator penetration and collimator and crystal scatter can significantly degrade the image quality and quantitative accuracy in situations such as imaging using isotopes emitting medium and high-energy photons.

MC simulation methods [4]—[7] have proved to be very useful in the development and evaluation of models for these effects [8]. However, full MC simulation of the collimator-detector response is notoriously slow and extremely computationally demanding. Thus, it is currently impractical for the simulation of SPECT data, especially for evaluation and compensation methods using large sets of phantoms.

1.2 OBJECTIVE AND CONTRIBUTION

Photon-tracking MC simulations are widely used to examine issues like image bias and loss of contrast from penetration and scatter. Unfortunately, MC simulations of SPECT are time consuming. Two related methods of speeding simulations is the use of Angular Response Functions (ARFs) [9, 10], or Point Spread Functions (PSFs) [11]—[16]. The ARF is a function of the incident photon's direction and energy. It represents the probability that, for an energy window of interest, a photon will either pass through or interact with the collimator and be detected. When using ARFs the detected position is approximated as the intersection point of the detection plane and the photon's direction vector. The ARFs require pre-computation using full MC simulations of point sources and provide fast modeling of the collimator-detector system. The PSF modeling can also be used as a Probability Density Function (PDF) in the MC simulator in order to avoid detailed tracking inside the complex collimator geometry. Both methods are used to speed up the MC simulation including modeling of the collimator-detector system, but the ARF method is more accurate as it is based on tracking photons through the collimator-detector system. We are currently in the process of adding an ARF feature to our public domain emission tomography simulation SimSET. In this thesis, we report on the generation of ARFs for ^{67}Ga, and their implications for quantitative imaging.

We choose Gallium-67 because it is clinically used for tumor imaging, but the quantitative accuracy of the image is not well established [17]. ^{67}Ga is challenging to image, with gamma emissions at ten different energies from 90 to 900 keV. In our clinic, we use three energy windows centered around the three most abundant energy peaks.

Generation of ARFs is extremely computational intensive: a table is needed for each incident energy, for each collimator/detector combination, and for each energy window of interest. The method is only useful when the same collimator/detector/energy window combination will be used for a large number of simulations. In this thesis, we report a systematic way to reduce the number of tables needed, and the number of photons needed to generate a table. Our method makes ARFs practical for a wider range of application.

1.3 ORGANIZATION

This thesis is structured into the following six chapters to clearly explain our work on standardizing ARF table pre-calculation requirements for collimator-detector response modeling in SPECT imaging:

- Chapter 1: This chapter includes the background, motivation, objective and contribution of our work to the Nuclear Medicine field.
- Chapter 2: This chapter gives a background introduction on SPECT imaging system, especially the gamma camera and its degrading factors.
- Chapter 3: This chapter introduces the Monte Carlo Simulation method, and the different simulation software that we used in this thesis work.
- Chapter 4: This chapter describes the parameterization method of the ARF tables and examining the ARF tables for Gallium-67 to study the influence from scatter and penetration.
- Chapter 5: This chapter presents a detailed methodology of generating ARF tables for realistic MC simulation based on our proposed estimation algorithm to reduce the pre-calculation requirements, and reports on the SimSET simulation and experiment results comparison.
- Chapter 6: This chapter summarizes the thesis work.

Chapter 2. SPECT IMAGING

2.1 SPECT GAMMA CAMERA

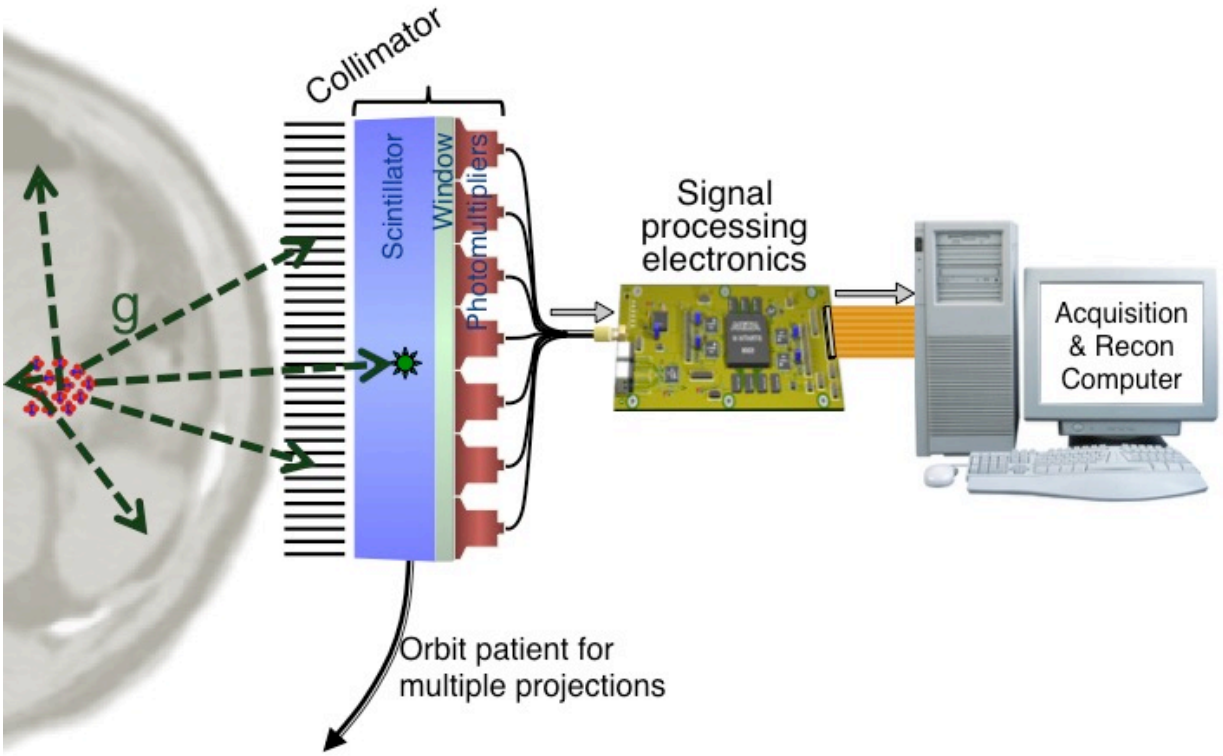

Figure 2.1. Basic principles and components of a modern gamma camera.

Single Photon Emission Computed Tomography (SPECT) uses a rotating gamma camera to acquire data for computed tomographic (CT) images [1]. This approach to tomography is employed with radionuclides that emit single γ rays or multiple γ rays with no angular correlations. Most of the commercially available SPECT systems are based on the gamma camera detector mounted on a rotating gantry. Figure 2.1 illustrates the basic principles of image formation with the gamma camera. The major components of a gamma camera are a collimator, a large-area NaI(Tl) scintillation crystal, a light guide, and an array of photo-multiplier (PM) tubes. The collimator usually consists of a lead plate containing a large number of holes and is used to define the direction of the detected γ rays. Four basic collimator types are used with the gamma camera: pinhole, parallel-hole, diverging and converging. The collimator forms a

projected image of the controlled γ-ray distribution on the surface of the NaI(Tl) crystal. The NaI(Tl) crystal is then viewed by an array of PM tubes, and signals from the PM tubes are fed to electronic or digital position logic circuits to determine the X-Y location of each scintillation event using the weighted average of the PM tube signals. The gamma camera acquires two-dimensional (2-D) projection images at equally spaced angular intervals around the patient in SPECT imaging. These images provide the 1-D projection data needed for reconstructing cross-sectional SPECT images, and reconstructed on a matrix of typically 64 × 64 or 128 × 128 pixels. A stack of contiguous 2-D images that form a 3-D image volume are constructed from cross-sectional images produced for all axial locations (slices) covered by the field of view (FOV) of the gamma camera.

Figure 2.2. The dual-headed GE Discovery NM/CT 670 SPECT/CT System

The typical sensitivity of a gamma camera is ~ 10^{-4}, meaning that 1 out of 10,000 emitted photons will actually traverse the collimator and be detected. A modern gamma camera (see Figure 2.2) consists of several detector heads, which contain a collimator and a detector, to improve the sensitivity of the SPECT system. Both dual-headed and triple-headed SPECT systems are available, with dual-headed systems being the most commonly used. Allowing two or three angular projections to be acquired simultaneously, these systems record each projection two or three times for the same total data acquisition time, and increase the total number of counts acquired for the image by twofold or threefold. Alternatively, a multi-head system can be used to acquire the same number of counts in half or a third of the time needed with a single-head system. An increasing number of SPECT systems are integrated with an x-ray CT scanner

(see Figure 2.2). These hybrid imaging systems are capable of acquiring SPECT images along with spatially registered CT images in quick succession.

The typical energy resolution of scintillation detectors used in modern gamma cameras is about 10% for the low energy windows (100 – 200 keV). Thus, by applying a photo-peak window, one can only discriminate a limited extent between unscattered photons (primary photons) and scattered photons that have lost energy. The width of the energy window has to be set to normally 15 – 20% of the photo-peak energy to collect a large fraction of primary photons. Therefore, a significant fraction of the photons detected in the energy window have been scattered, reducing the resolution and quantitative accuracy of the final image.

2.2 IMAGING DEGRADATION FACTORS IN SPECT

Ideally, there should be a linear relationship between the signal level for a voxel in a SPECT image and the amount of activity contained within the volume of tissue in the patient that corresponded to the location of the voxel. This would be useful for both quantitative applications, such as perfusion studies, and for visual interpretations of the image. In practice, this ideal result is not achieved because of several image degradation factors, which do not match the idealized assumptions made for the development of reconstruction algorithms. To avoid this, one must either use somewhat modified approaches to data acquisition or apply post-processing of the acquired data.

The attenuation of γ rays in SPECT imaging is mainly the result of Compton scattering and depends on the distance the γ rays have to travel through the tissue to reach the detector, the type of the material and the photon energy. The attenuation of a narrow beam of photons passing through a non-homogenous medium of thickness *d* is given by:

$$\psi = \psi_0 \exp\left(-\int_0^d \mu(r)dr\right) \tag{2.1}$$

where ψ is the photon flux after attenuation, ψ_0 is the incident photon flux and μ is the linear attenuation coefficient (the total sum of all possible differential cross-sections). For 140 keV γ rays, the linear attenuation coefficient of tissue is 0.155 cm^{-1}; therefore γ rays that are emitted from a depth of 10 cm in the body would only have a probability of 0.21 ($e^{-10\times0.155}$) of emerging from the body in their original direction.

Because the collimator holes are not infinitely narrow and certain photons may cross the septa walls, the photons that traverse through the collimator will not come from a direction that is exactly aligned with the holes. This results in a substantial loss of resolution in the images and reconstructions. A collimator with a thick width or septa wall can decrease the collimator blurring but it would also greatly reduce the sensitivity of the collimator. Therefore, a compromise has to be made between collimator resolution and sensitivity. Several types of collimators have been developed to achieve this compromise, such as parallel collimator, fan beam collimation and pinhole collimation. Another design variable for collimators is the energy of the targeted photons. Different types of collimators are used for photon energies: Low Energy All-Purpose (LEAP), Low Energy High Resolution (LEHR), Medium Energy General Purpose (MEGP) and etc. In this thesis we present a characterization of MEGP parallel collimator by using MC simulations.

Another important image degrading factor in SPECT is scattering. Scatter results in the detection of "incorrect" photons and it is also a cause of attenuation. A photon can penetrate the matter without interaction, or it can be absorbed, or it can scatter and lose part of its energy. If a scattered photon is detected in the energy window, it will suggest an incorrect emission point and cause severe degradation of the contrast and quantitative accuracy of the reconstructed image.

Statistical noise is also present in the imaging process, because the detection of photons in Nuclear Medicine is a Poisson process. The low detection rate ~10^{-4} and the huge number of emitted photons suggest that there is a significant amount of Poisson noise measured. The signal-to-noise ratio (SNR) is defined as the ratio between the noise (the square root of the variance) over the mean:

$$\mathrm{SNR} = \frac{\sqrt{Var(N_A)}}{N_A} = \frac{\sqrt{N_A}}{N_A} = \frac{1}{\sqrt{N_A}} \tag{2.2}$$

Since the variance of Poisson noise in the detector bin A is proportional to the mean of counts N_A, the acquisition of a large number of counts will increase the SNR. However, the number of counts is small because it is proportional to: the length of the scan, the radiation dose injected to the patient, the size of the detector bin, and the number of camera heads. Thus, a low SNR is inherent to the SPECT image and noise is a major cause of image degradation.

There are other instrumentation-related factors influencing the quality of SPECT images, such as the non-linearities and non-uniformities of the detector, and inaccuracy of the center of

rotation of the detector. Also, the image quality can be greatly affected by biological factors, such as tracer kinetics and target specificity, and by patient or organ movement during the acquisition process.

Chapter 3. MONTE CARLO SIMULATION

3.1 MONTE CARLO METHOD

Monte Carlo (MC) numerical simulation methods are statistical methods that based on using random numbers to perform simulation of any specified situation [18]. Because of the close connection to games based on chance and the location of a very famous casino in Monte Carlo, its name was chosen during World War II Manhattan Project. In most MC applications, the physical process is simulated directly from known probability density functions (PDFs). The simulation can be made by random sampling from the PDFs, if these PDFs can be defined accurately. To obtain an accurate estimate of the parameters to be calculated, a large number of simulations of histories, such as photon or electron tracks are necessary.

Simulations studies have several advantages over experimental studies. It is very convenient to change various parameters and investigate the performance of the system affected by these changes. Therefore simulations are important to the optimization of an imaging system. One can also study the effects of the parameters that cannot be measuredly directly in the experiment. For instance, it is impossible to separately measure the scattered and unscattered components of the emitted radiation from the unscattered component of a distributed source. The MC technique, however, can incorporate the known physics of the scattering process, and make it possible to simulate scatter events from the source and determine their effect. Thus, with all details of the simulation accessible, a simulation program can greatly assist to understand the underlying processes.

Generally speaking, MC simulations can be very time consuming, especially when most of the photon histories generated are likely to be rejected. For example, the probability that a photon hits the detector is usually less than 1 in 100,000 when simulating a point source at a large distance from a small detector. Variance Reduction techniques can be applied to improve the efficiency of the simulation and statistical properties of the produced images. These techniques calculate the photon history weight, W, which represents the probability that the photon can pass through a particular history of events. Based on assuming probability functions of the physical processes, these techniques can either reduce the variance per history or allow more histories to be simulated during the same CPU time, thus speed up the simulation. The

photon is then associated with a weight *W*, which is the quotient between the true probability density and the fictitious probability density, to correct for the speed up.

3.2 THE SIMIND PROGRAM

The SIMIND version 5.0 [22], which is developed by Professor Michael Ljungberg, Medical Radiation Physics, Department of Clinical Sciences, Lund, Lund University, Sweden, is used in this thesis. It is a photon-tracking MC simulator that includes models for many different collimators. The entire code is written in Fortran-90. It can be freely downloaded from http://www.radfys.lu.se/simind and includes versions that are fully compatible with most major operation systems, i.e. Linux, Mac OSX, and Windows.

We simulated a parallel hole collimator using both SIMIND geometric and photon-tracking collimator models with moving collimator approximation, which averages response over all collimator hole positions. We used SIMIND's listmode output option and processed the output in Python scripts to get the desired ARF tables as described in Chapter 4.

3.3 GATE SIMULATION TOOLKIT

GATE, the Geant4 Application for Tomographic Emission, is an advanced opensource software package developed by the international OpenGATE collaboration and dedicated to numerical simulations in medical imaging and radiotherapy [19]. GATE, which consists of several hundred C++ classes, combines the advantages of the well-validated physics models from Geant4 simulation toolkit, sophisticated geometry description, and powerful visualization and 3D rendering tools with original features specific to emission tomography.

On the SPECT side, GATE is capable of simulating a realistic system with a collimator composed of thousands of aligned holes. The photon tracking process includes transportation, septal penetrations and interactions such as Compton scattering, photoelectric absorption and x-ray fluorescence (which can occur in the collimator or detector and be detected in some energy windows). Thus, it is a very tedious and computationally demanding task even with the modern computation power. For realistically modeled parallel hole collimators used in SPECT MC simulations, the probability of a photon being detected in the crystal part of the detection system after penetrating the collimator surface is only one in a thousand. Moreover, the collimator-

detector response, which is a function of the source distance and includes septal penetration, scatter and x-ray fluorescence, is a significant image degradation factor in SPECT imaging.

In the next chapter, we implemented the methodology designed by X. Song et al [20], which relies on the use of Angular Response Function (ARF) for the collimator-detector system, to significantly decrease the time required for collimator modeling.

3.4 THE SIMSET PROGRAM

The Simulation System for Emission Tomography (SimSET) [21], a photon-tracking MC simulation, has been developed in the Imaging Research Laboratory at the University of Washington over the last 20 years and used widely in the Nuclear Medicine research field. SimSET enables a precise and efficient modeling of physics phenomena and basic detector designs, and provides a fast photon transport simulation in both SPECT and PET. The availability and modular structure of the source code, the well-known language of the code (C), and the reliability of the program on different computer platforms, i.e. Linux, Unix, Windows, etc., makes it easy to modify and incorporate the ARF into the Collimator Module.

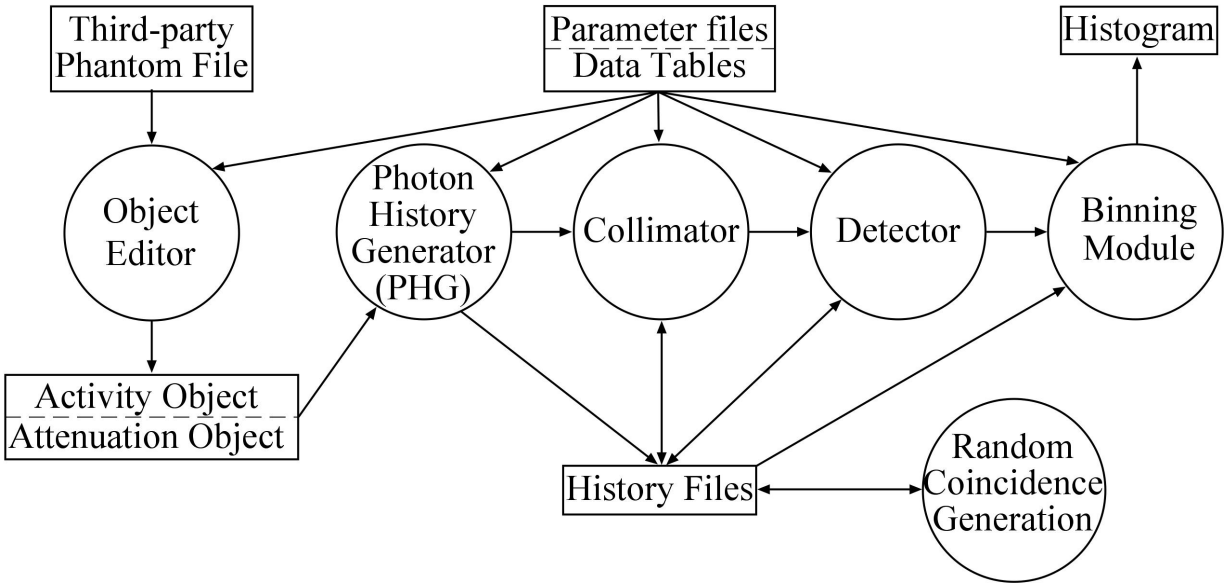

Figure 3.1. The main software modules and data flows for the SimSET software. (From SimSET website.)

Figure 3.1 shows the modular structure and data flows of SimSET program. A typical simulation proceeds decay by decay: the photon history generator generates a decay and the produced photon(s), then tracks the photon(s) through the phantom, the collimator and detector in a sequence. Finally the binning module histograms the detected events into a user defined output format. The experienced user may modify some of the modules for specific simulation purpose. In this thesis, we are in the process of modifying the Collimator Module, which performs the collimation process, because in the original SimSET version only the geometrical component of the collimator is modeled. A set of ARF tables will be used to replace tracking the photons through the collimator and detector. The modified SimSET program will be able to realistically model parallel hole collimation including septal penetration, scatter and x-ray fluorescence, giving a more accurate collimator-detector response. Moreover, the usage of pre-computed ARF tables will significantly speed up the simulation process and improve the efficiency.

Chapter 4. ANGULAR RESPONSE FUNCTION GENERATION

4.1 ANGULAR RESPONSE FUNCTION PARAMETERIZATION

We computed the ARF tables using the method described by X. Song et al [9] for every combination of chosen point source energy and energy window. The ARF is a function of the polar and azimuthal angles of the incident photon with the collimator surface, and it describes the probability that an incident photon hitting the collimator would be detected in an energy window of interest. The tables are parameterized by the azimuthal and polar angles as shown in Figure 4.1.

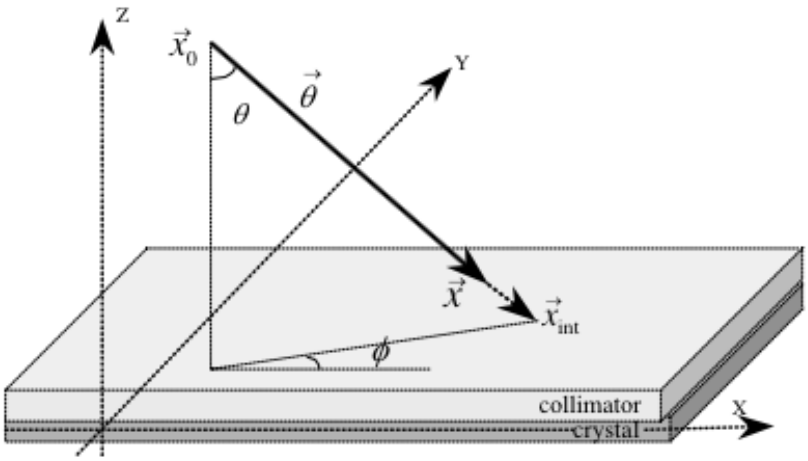

Figure 4.1. The polar (ϕ) and azimuthal (θ) angles. (From X. Song et al [9].)

The table parameterization is based on the cosine of the azimuthal angle and the tangent and cotangent of the polar angle, as shown in Table 4.1 and 4.2. Table entries are normalized by solid angle.

Table 4.1. Parameterization of ARF as a function of cos θ. (From X. Song et al [9].)

Bins	Range of cos θ values	Sampling intervals Δ cos θ
0-1023	1.00-0.99	0.000 009 7656
1024-1535	0.99-0.95	0.000 078 125
1536-1791	0.95-0.75	0.000 781 25
1792-2047	0.75-0.00	0.002 929 69

Table 4.2. Parameterization of ARF as a function of tan ϕ and cot ϕ. (From X. Song et al [9].)

Bins	Sampling for	Sampling range	Sampling intervals	Corresponds to the polar angle
0-255	tan ϕ	0-1.0	Δ tan ϕ = 0.039 06	0 – 45°
256-511	cot ϕ	1.0-0	Δ cot ϕ = 0.039 06	45 – 90°

4.2 Angular Response Functions in MC Simulations

In this thesis, we use two methods to generate ARFs in MC simulations with SIMIND or GATE respectively. Both of the methods are based on the GE Discovery 670 SPECT/CT system shown in Figure 2.2. We use GE-Infinia-MEGP collimator, which has the same characteristics as the collimator that we use in our clinic. There are two different axial thickness type of the photon-tracking SPECT collimator. Shown in Figure 4.2, type (a) has a single septal thickness, type (b) has double septal thickness. We use SIMIND to model the collimator as type (a) and GATE to model the collimator as both type (a) and type (b). They share the same hole width w, the septal thickness t, and type (b) can have a glue gap p. We did not model the glue gap (p = 0).

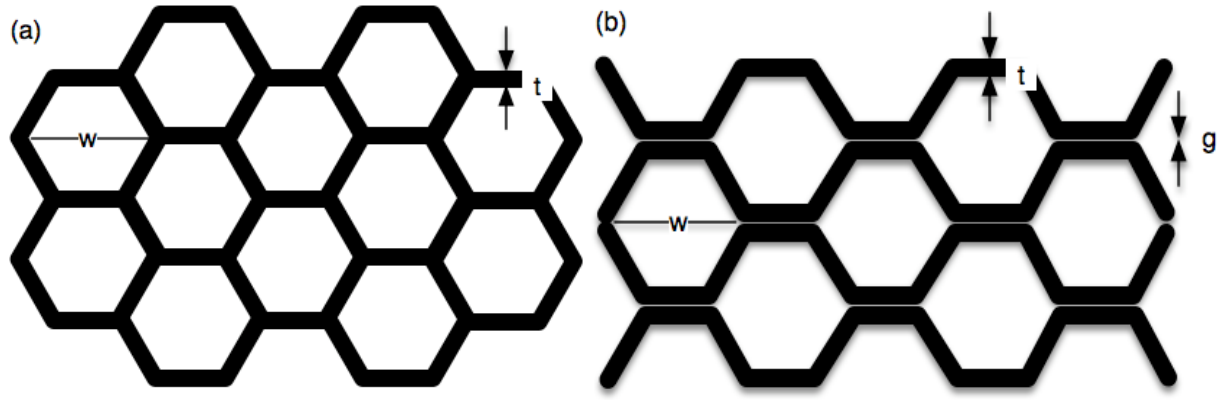

Figure 4.2. In-plane geometry parameters for the two different axial thickness types of the photon-tracking SPECT collimator.

In SIMIND, the detector consists of a 0.95 cm thick NaI crystal with a 0.2 cm aluminum cover and 5 cm backscatter compartment behind. The tomograph is simulated with an intrinsic spatial resolution of 0.37 cm, and an energy resolution of 9.5% Full Width Half Maximum (FWHM) at 140 keV.

The ARF is a function of the incident photon direction and energy and represents the probability that a photon will either interact with or pass through the collimator, and be detected at the intersection of the photon direction vector and the detection plane in a targeted energy window. In SIMIND, a point source at each of the nine ^{67}Ga γ ray emission energies is used. The listmode output is obtained and fed into our Python scripts to process into the tabulated ARF format. In GATE, the ARF generation includes two steps. In the first step, the data needed to generate the ARF tables are computed from a rectangular source located at the center of the field of view (FOV). In the second step, the ARF tables are calculated and stored in a binary file from the raw data generated in the first step. The ARF tables depend strongly on the distance from the detector to the source used in the previous step.

4.3 ^{67}Ga Characterization

Table 4.3. ϒ ray abundance for ^{67}Ga.

Gamma Ray Energy (keV)	Mean Number / Decay (%)
91.3	3.07
93.3	38.30
184.6	20.90
209.0	2.37
300.2	16.80
393.5	4.70
494.2	0.0686
703.1	0.0105
794.4	0.0513
887.7	0.1450

Gallium-67 is clinically used for tumor imaging, but the quantitative accuracy of the image is not well established [23]. Despite the increasing use of ^{18}F-fluorodeoxyglucose (FDG) for Positron Emission Tomography (PET) imaging of lymphoma, conventional SPECT imaging of ^{67}Ga remains important for both the evaluation and staging of lymphoma and for the imaging of infection [24]—[26]. Because FDG PET is currently available only in a relatively small number

of mostly industrialized countries, ^{67}Ga, with its 78 hours half-life and less costly imaging requirements, plays an essential role in many regions of the world. Table 4.3 shows the relative abundance of the ten ϒ ray emissions for ^{67}Ga. We simulated a point source at each of these energies. The energy decay scheme of ^{67}Ga is characterized by principal photon emissions at 91.3 and 93.3 keV (41.37% abundance), 184.6 keV (20.90%), 209 keV (2.37%), and 300.2 keV (16.80%). High-energy photons are of low abundance (4.7% at 393.5 keV, less than 1% for all others), yet these contaminant photons have an increased probability of penetrating through, or scattering in, the collimator and/or crystal and contributing to other photo peaks as down-scatter. Furthermore, lead X-rays produced in the collimator also contribute significantly to the counts detected in the 93.3 keV energy window. In the remainder of this Chapter, we shall focus on examining the influence of these many sources of contamination on SPECT images.

4.4 ^{67}GA IMAGING CONTAMINATION

We first used SIMIND [22] to simulate a point source at each of the ten ^{67}Ga emission energies. The activity was simulated either 200 cm or 10 cm above the center of the face of the collimator. We based on our simulation on the GE Discovery 670 SPECT/CT system. The parameters for the GE Infinia-MEGP collimator and the detector in our simulation have been described previously. We created a +/- 10% symmetric energy window around each of the three energy peaks used for ^{67}Ga imaging in the clinic: 93.3 keV, 184.6 keV, and 300.2 keV. For each emission energy, a sum of all events over the whole detector for both the geometric and photon-tracking collimators was computed. We defined *G(E,W)* and *P(E,W)* to be the contribution of photon emitted with energy *E* to the window centered at *W* for the geometric and photon-tracking collimator simulations respectively. We defined the contamination as a percentage of true signal to be:

$$C(E,W) = \begin{cases} \frac{A(E)\times P(E,W)}{A(W)\times G(W,W)} & if\ E \neq W \\ \frac{A(E)\times (P(E,W)-G(E,W))}{A(W)\times G(W,W)} & if\ E = W \end{cases} \tag{4.3}$$

where A(E) is the abundance taken from Table 4.3. We defined the penetration and scatter to total ratio to be:

$$R(E,W) = \frac{P(E,W)-G(E,W)}{P(E,W)} \tag{4.4}$$

In Figure 4.3, we plot the contamination from Equation (4.3) by emission energy for each energy window. Despite its low abundance, we notice that the 887.8 keV photon is a major contaminant, particularly in the 300.2 keV window. In the 93.3 keV window the biggest contaminant is the 91.3 keV emissions, which could also be considered as part of the true signal. In the other two windows, the largest contaminant is from photons at the window energy. In Figure 4.4, we plot the Equation (4.4) by emission energy for each energy window. In all three windows, penetration and scatter contribute to the great majority of contamination from photons emitted with energies over 390 keV.

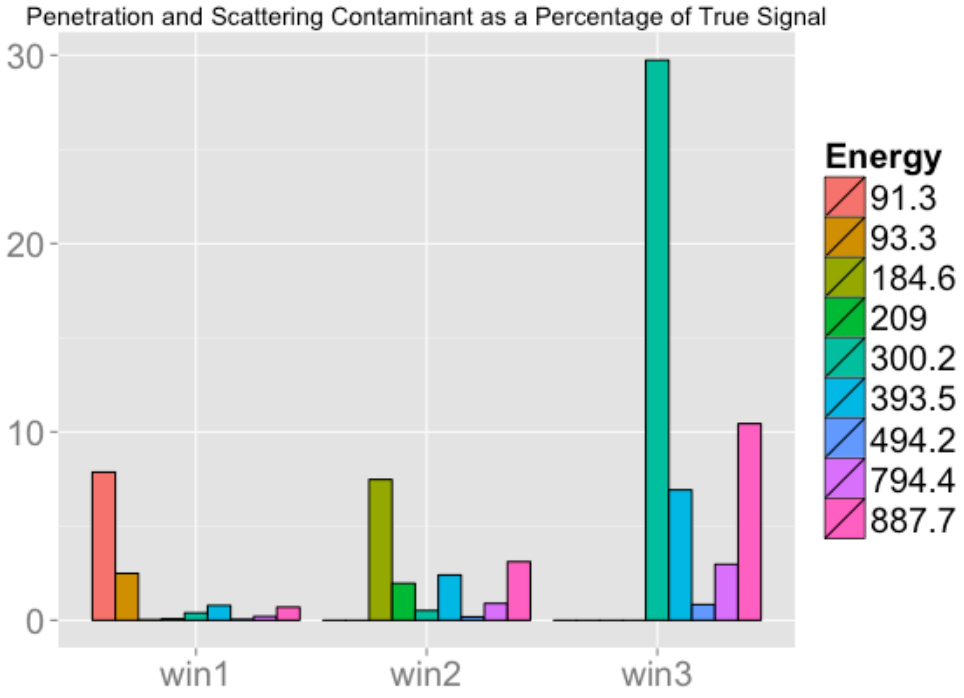

Figure 4.3. Penetration and scatter contamination from each emission energy in the energy windows centered at 93.3 keV (Win1), 184.6 keV (Win2), and 300.2 keV (Win3).

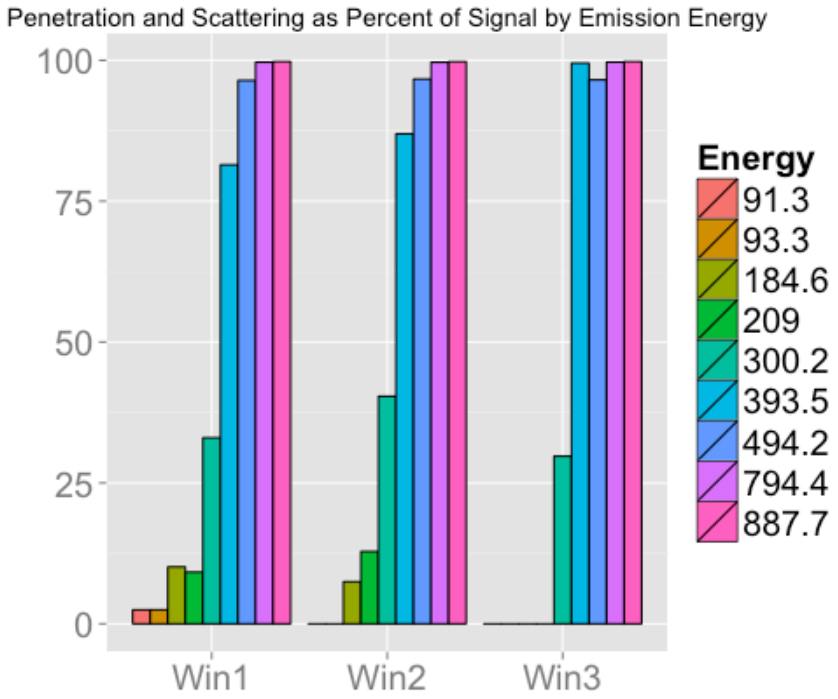

Figure 4.4. Penetration and scatter contamination from each emission energy in the energy windows centered at 93.3 keV (Win1), 184.6 keV (Win2), and 300.2 keV (Win3).

We computed ARF tables for every combination of emission energy and energy window. The tables are parameterized by the cosine of the azimuthal angle θ and the tangent and cotanget of the polar angle ϕ as described in Section 4.1. In Figure 4.5 and 4.6, we show the ARFs for the photon energies of 300.2 keV and 887.8 keV in the energy window centered at 300.2 keV. We see 15.8 % as many 887.7 keV photons as 300.2 keV photons will be detected in the energy window at 300.2 keV. Note that the simulations shown above did not model a backscatter compartment. We are expecting to see more contamination from the higher energies in the following simulations with the backscatter compartmented included.

In sum, there is significant contamination from collimator penetration and scatter for ^{67}Ga imaging. We note that our ARF tables are derived from simulation of point sources in air. However, in patient imaging, there will be significant additional contamination from scatter in the patient, the backscatter compartment and other confounding factors.

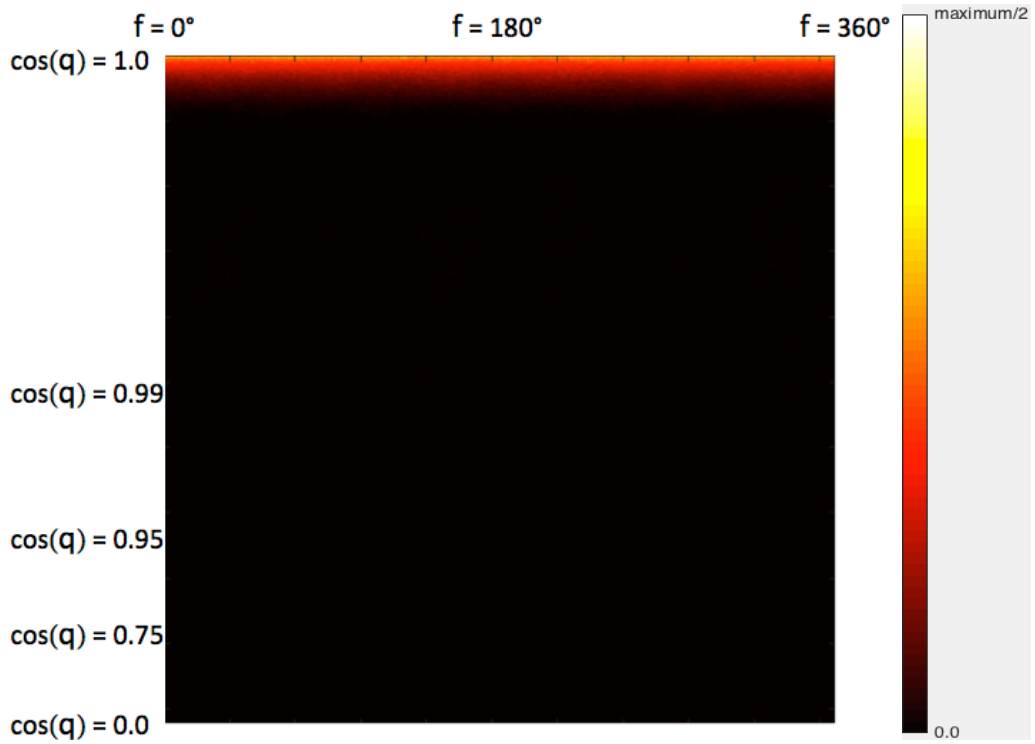

Figure 4.5. Angular response tables for photon energy 300.2 keV in the energy window centered at 300.2 keV.

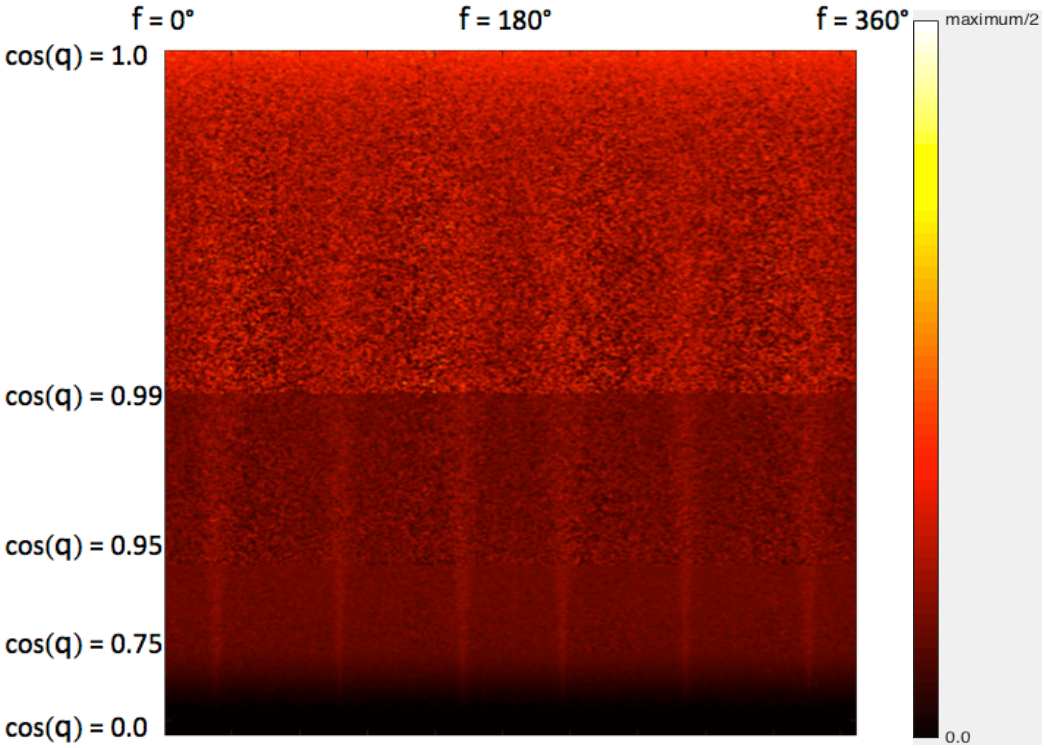

Figure 4.6. ARF table for photon energy 887.8 keV in the energy window centered at 300.2 keV.

Chapter 5. ANGULAR RESPONSE FUNCTION ESTIMATION

A tabulated model of the collimator-detector response was implemented and validated within the GATE framework to significantly reduce the simulation time required to produce ARF tables for SPECT simulation [27]. In this chapter, we use the ARF-based model of the collimator-detector response for SPECT simulations within GATE for ^{67}Ga. Considering the simulation of the GE Discovery 670 SPECT/CT system using medium energy general purpose (MEGP) collimators, we examine the ARFs for each incident energy and for each energy window of interest. We look both at the number of photons needed to get an adequate estimate of an ARF table and at our ability to estimate an ARF for a given incident energy and energy window from ARFs with nearby incident energies for the same window. We find that we can reduce the ARF pre-calculation requirements by using fewer tables and less photons to generate the tables.

5.1 ^{67}GA ARF TABLE CHARACTERISTICS

The ARF tables are tabulated as a function of the cosine of θ, the azimuthal angle of incidence, and the tangent and cotanget of φ, the polar angle of incidence. We used type (b) double-walled GE-Infinia-MEGP collimator in Figure 4.2 (b) and a 1.0 cm thick NaI crystal with 0.7 cm glass backscatter compartment behind, and simulated an energy resolution of 9.0% FWHM at 140 keV. We created +/- 10% symmetric energy windows around the three energy peaks used for ^{67}Ga imaging in the clinic: 93.3 keV, 184.6 keV, and 300.2 keV. These ARF tables are calculated from GATE simulations. First, photons are emitted from a 2 × 1.2 cm rectangular source in air within a given incident energy window. The distance from the source to the collimator surface was set to 38.8 cm. This distance was chosen to average out the effects of the collimator hole pattern by letting the rectangular source cover several holes. The photons undergoing photoelectric absorption in the crystal with or without Compton interactions are collected. The deposited energy and corresponding incidence angles with respect to the collimator plane are stored, and the data are used to generate the ARF table for a given incident energy. Figure 5.1 shows the ARF table for 300.2 keV photons in the energy window from 270.18 to 330.22 keV. Figure 5.2 shows the ARF table for 887.7 keV photons in the same energy window. The cos θ varies between 1 and 0.8117, which corresponds to azimuthal angle θ from 0° to 35.74° and covers the collimator-detector surface area. The polar angle φ varies from 0° to 90°. In

comparison, 887.7 keV photons have more penetration and scatter contamination than 300.2 keV photons, and thus the 887.7 keV ARF table extends much further along the cos θ axis than the 300.2 keV table.

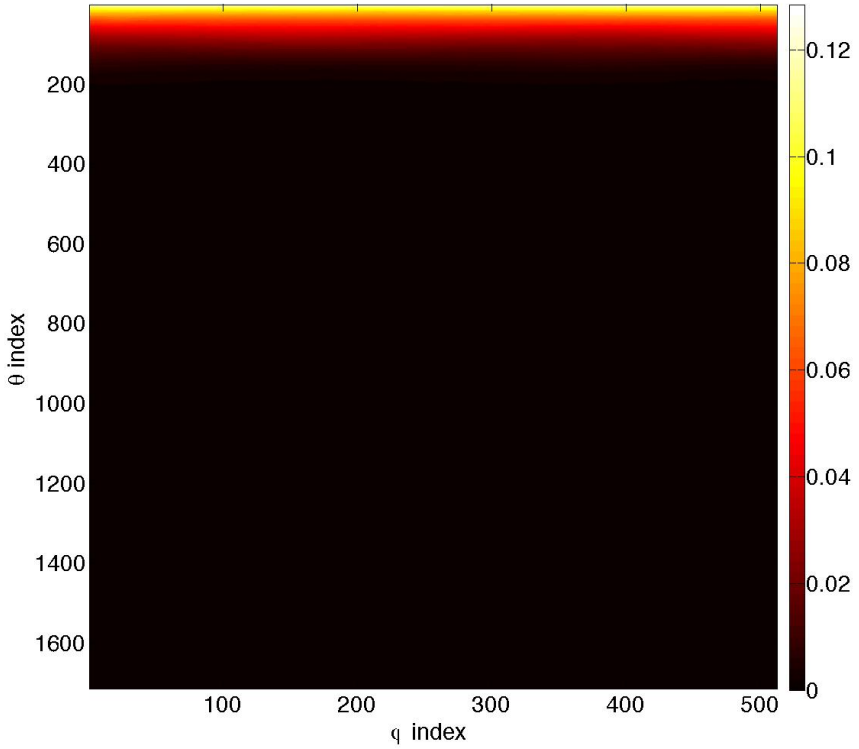

Figure 5.1. ARF table for 300.2 keV photons in the 270.18 – 330.22 keV energy window.

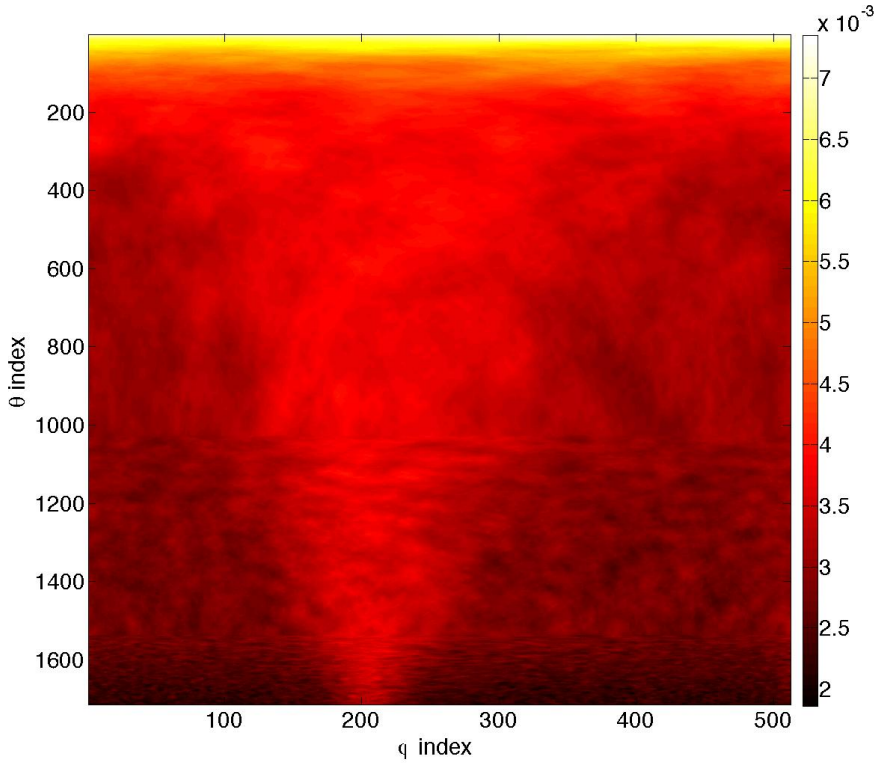

Figure 5.2. ARF table for 887.7 keV photons in the 270.18 – 330.22 keV energy window.

We examined characteristics of the ARF tables at each of the ten emission energies of ^{67}Ga: the backscatter energies at which 180° backscatter will hit the energy window's top/bottom energy as shown in Table 5.1; the full width maximum (FWM) energies around the peak; and some selected energies to fill in the gaps in between so that we can get a smooth curve along the targeted energy range. The FWM energies were calculated based on the full width half maximum (FWHM) points, which were calculated according to the rule that the energy resolution should ideally be proportional to $1/\sqrt{E}$, because the number of photoelectrons is proportional to the energy deposited in the crystal [1]. The FWM points are defined as twice the distance away from the peak energy than the FWHM points. For each table, we calculated the normalized amplitude of the whole table by adjusting the size of each bin:

$$A(E,W) = \int\int p(\theta,\phi)d\theta d\phi = \sum\sum \Delta cos\theta |\phi|_{\arctan(tan\phi)}^{\arctan(tan\phi+\Delta(tan\phi))}| \qquad (5.1)$$

where $p(\theta,\phi)$ is the probability for a specific bin at azimuthal angle θ and polar angle ϕ, and A(E,W) is the normalized amplitude for energy E and energy window W.

Table 5.1. Backscatter energies at which 180° backscatter will hit the energy window's top/bottom energy.

Energy In (keV)	Energy Deposited (keV)
194.35	83.97
221.18	102.63
305.22	166.14
350.91	203.06
430.52	270.18
499.23	330.22

We report the normalized amplitude at each selected energy as a percentage of the center energy in each energy window as shown in Figure 5.3, 5.4, and 5.5. The results for the 4-billion-decay ARF tables (i.e. green marks on plot) will be used to estimate ARF tables for other incident energies. The 100-million-decay tables points in red are used to get the accurate amplitudes at other energies. The summed horizontal and vertical profiles of all the 4-billion-decay ARF tables in the 83.97 – 102.63 keV energy window are shown in Figures 5.6 – 5.8. The profiles are scaled so that they have similar amplitudes, and the 512 points on the horizontal profile are clasped to 32 points by summing every 16 points in a row to reduce the influence from the noise in tables with low sensitivity. By examining the characteristics of the horizontal and vertical profiles, we group the tables into three families: 72.74—102.63 keV, 113.88—350.91 keV, 393.5—887.7 keV. The dividing energy between the first family and second family falls on the FWM point. The second family and the third family are divided at the point where penetration begins to dominate. The first family includes the curves around the peak energies; the second family includes the energies at the low sensitivity region; the third family includes the energies where penetration is dominating.

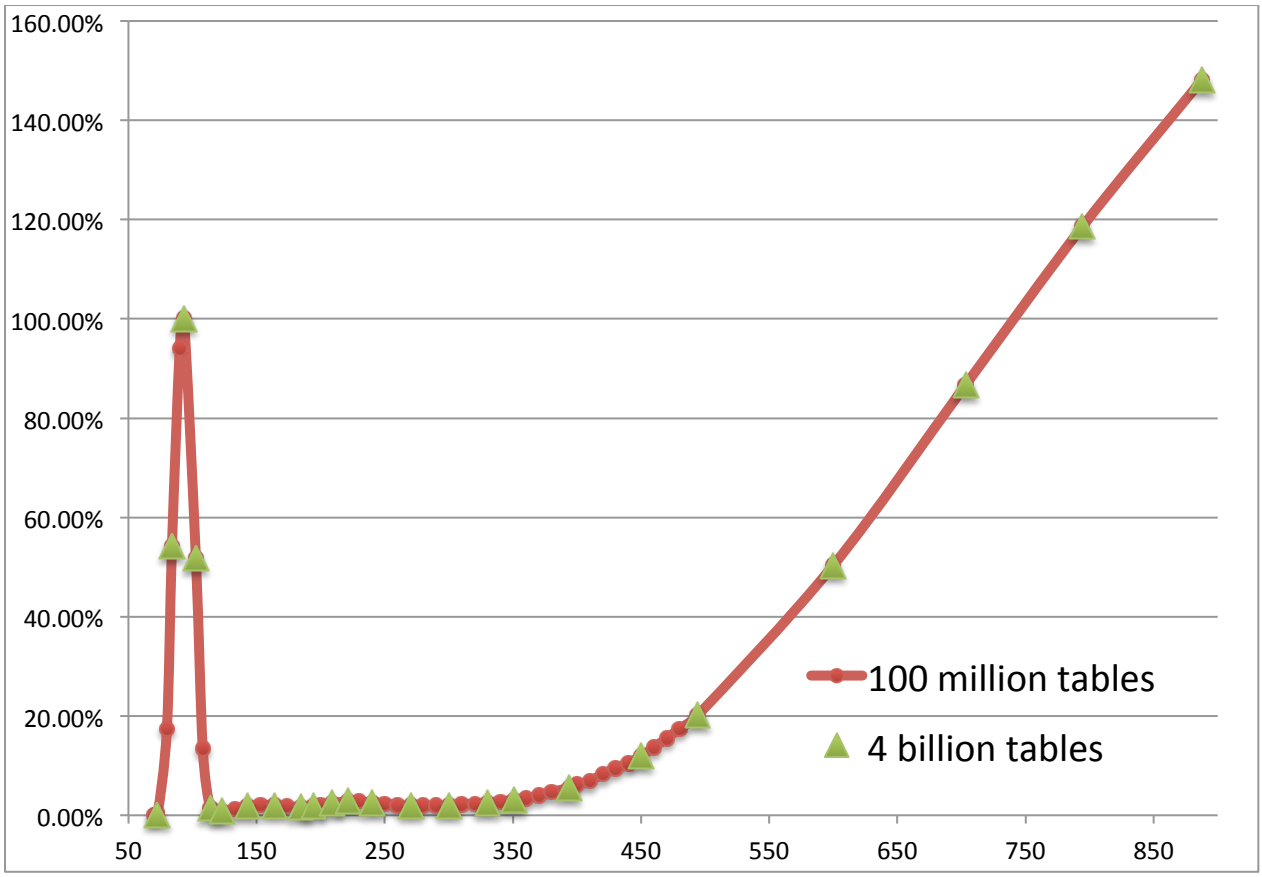

Figure 5.3. Percentage of the normalized amplitude to the center energy curve in 83.97 – 102.63 keV energy window.

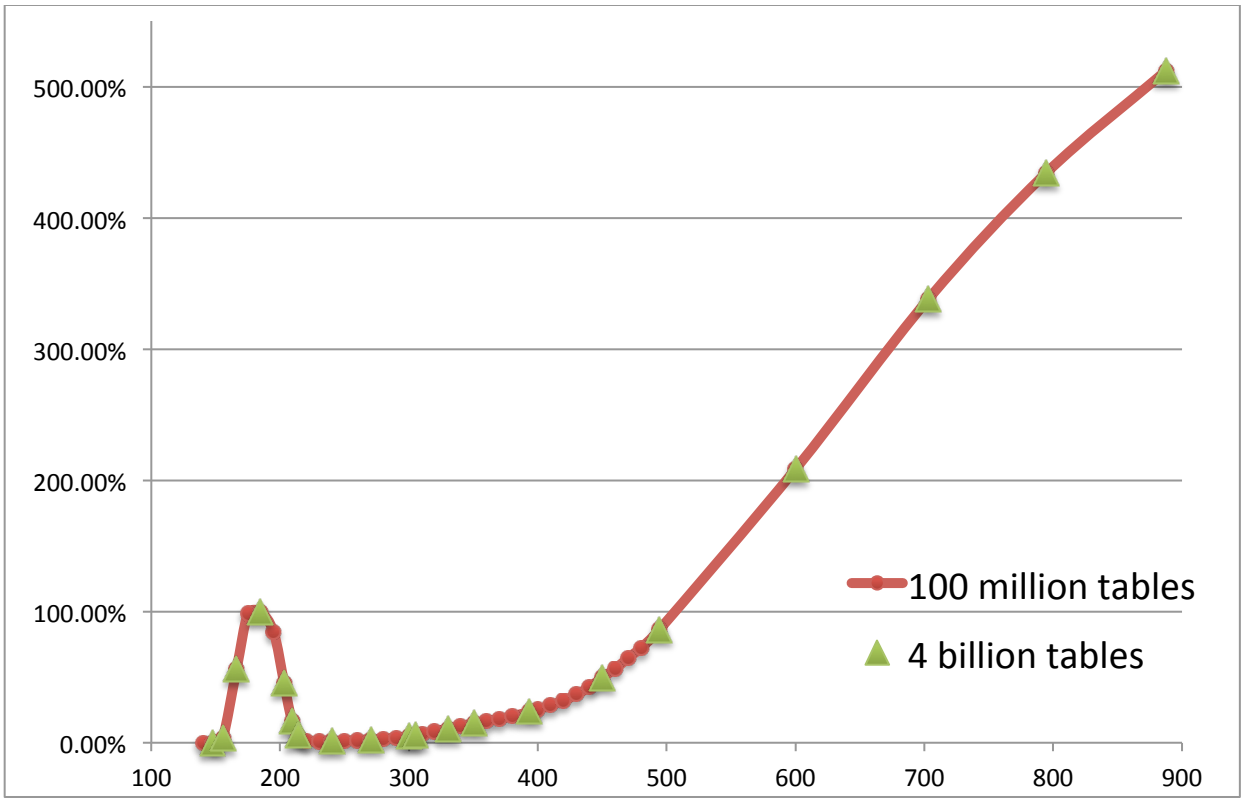

Figure 5.4. Percentage of the normalized amplitude to the center energy curve in 166.14 – 203.06 keV energy window.

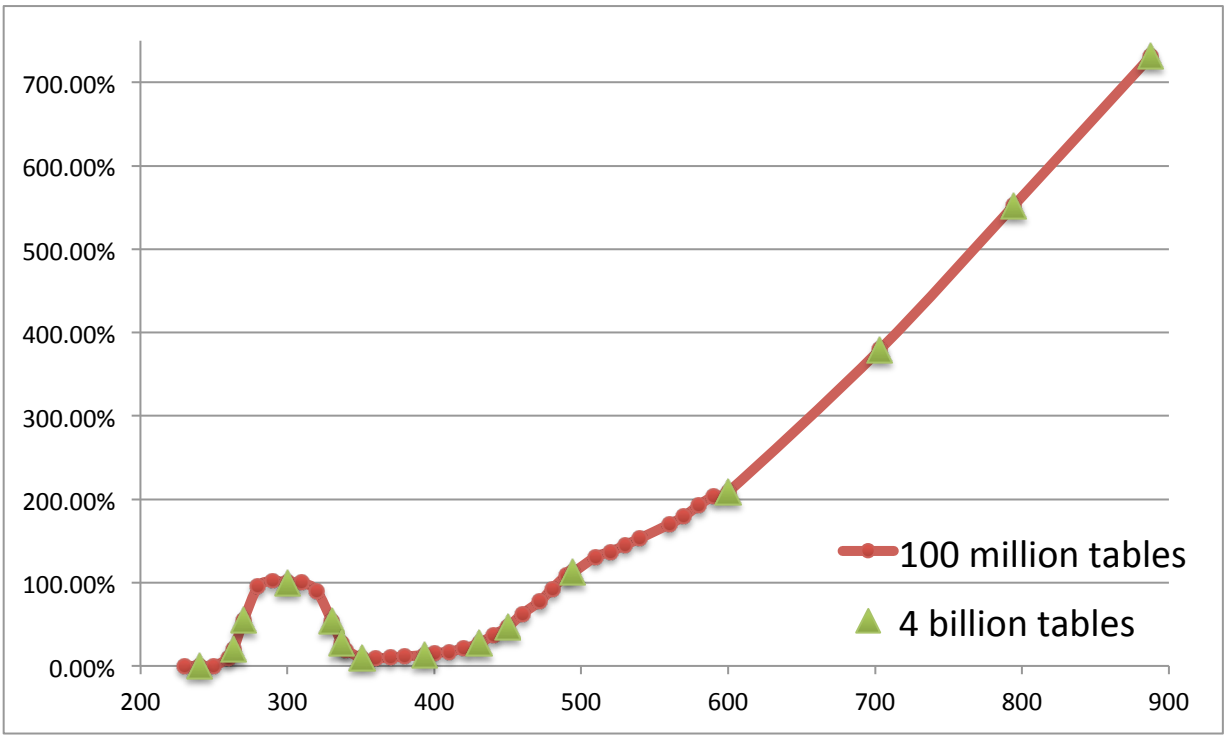

Figure 5.5. Percentage of the normalized amplitude to the center energy curve in 270.18 – 330.22 keV energy window.

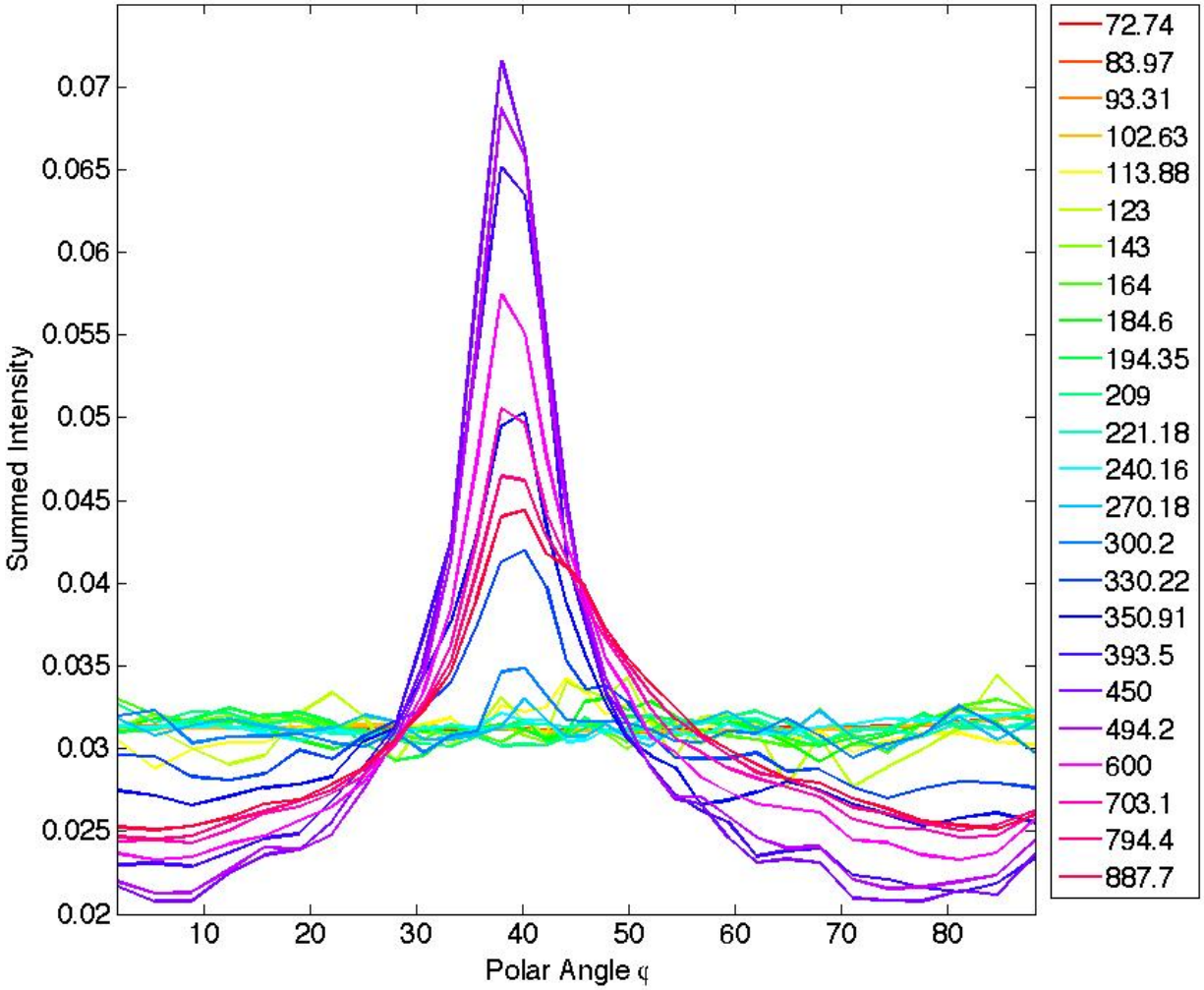

Figure 5.6. Summed scaled horizontal profiles of the 4-billion-decay ARF tables in 83.97 – 102.63 keV energy window.

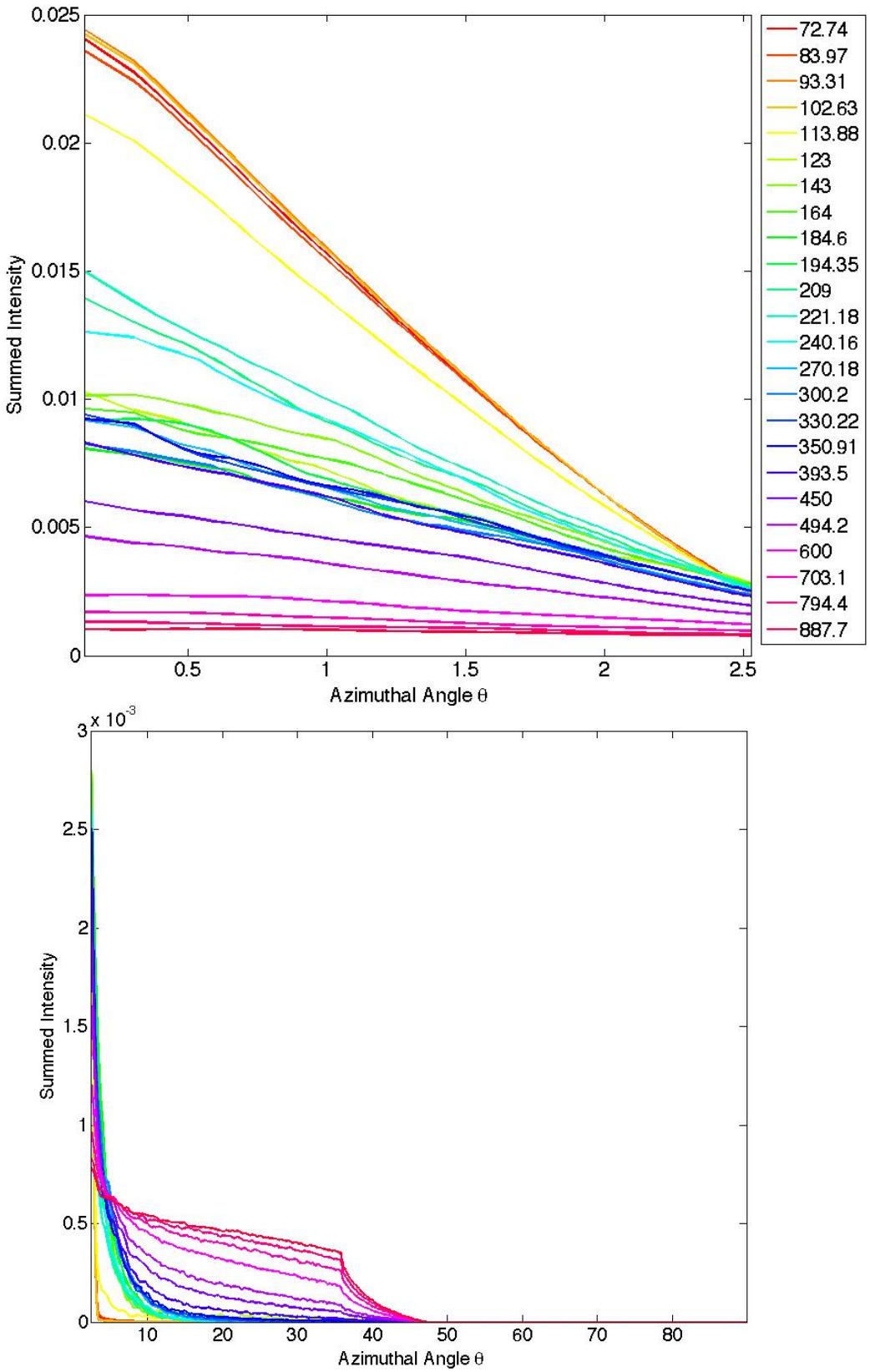

Figure 5.7. Summed normalized vertical profiles with azimuthal angle θ from 0° – 2.5° (top) and 2.5° – 90° (bottom) of the 4-billion-decay ARF tables in 83.97 – 102.63 keV energy window.

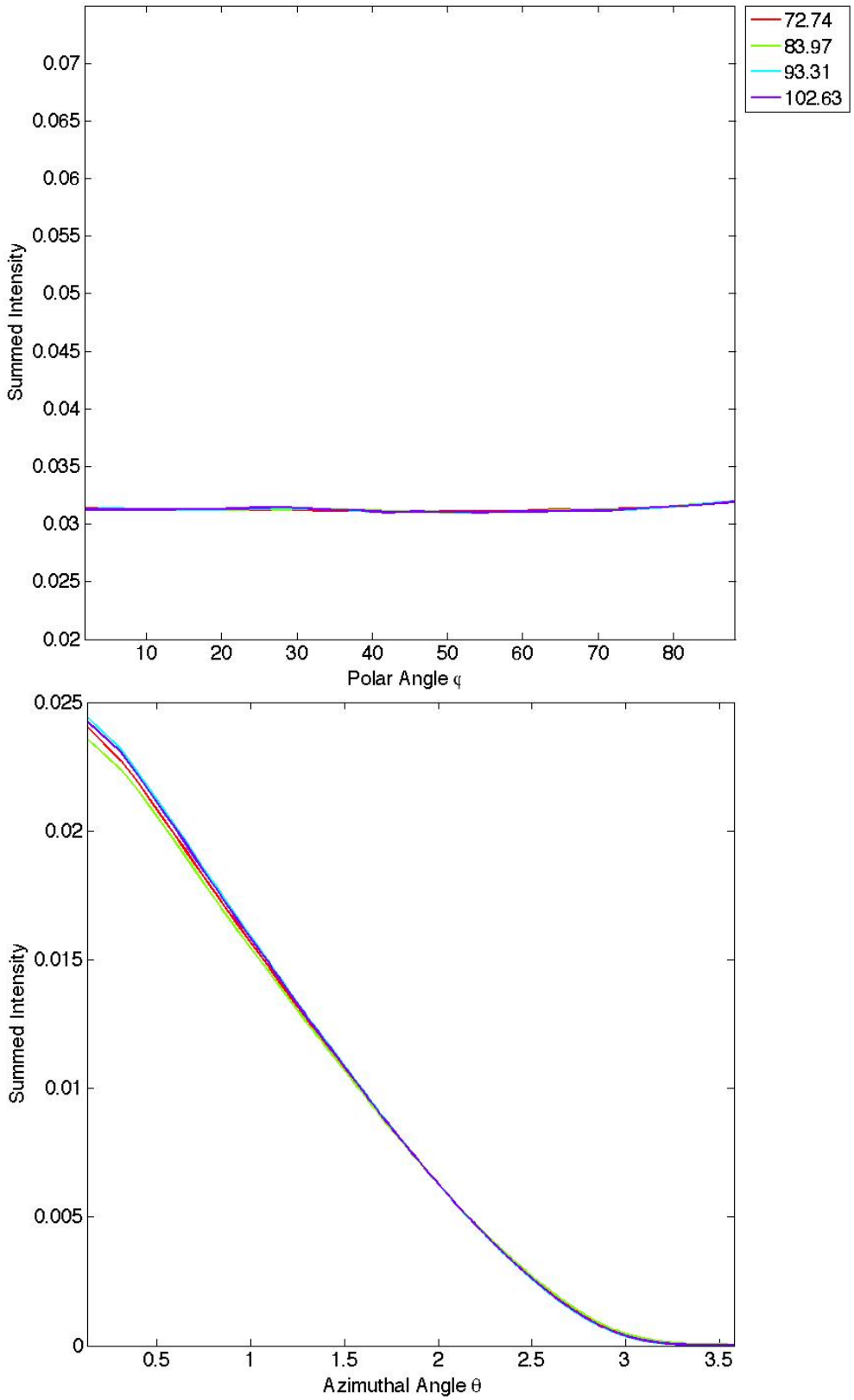

Figure 5.8. Summed scaled horizontal (top) and vertical (bottom) profiles of family 1: 72.74—102.63 keV ARF tables in 83.97 – 102.63 keV energy window.

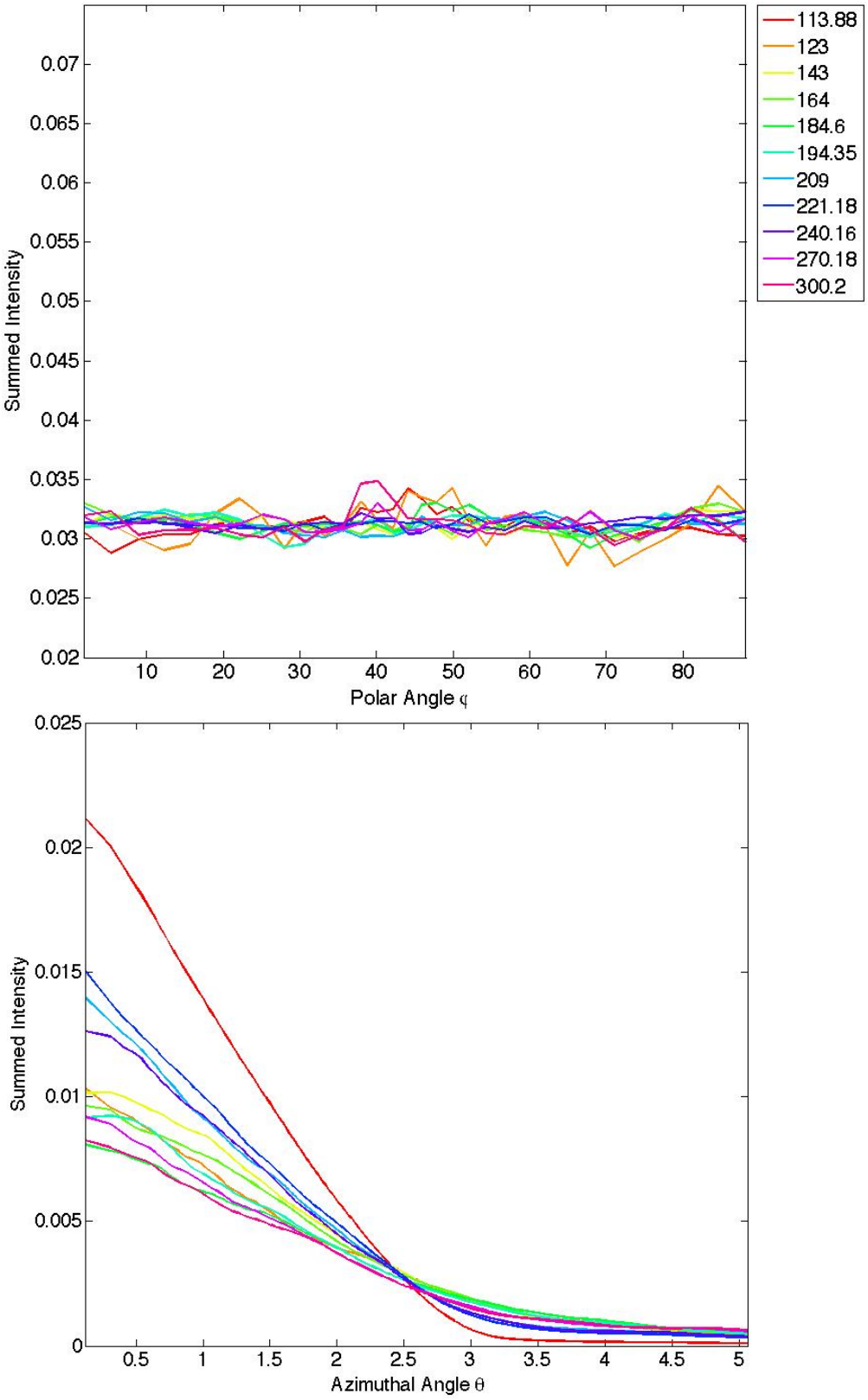

Figure 5.9. Summed scaled horizontal (top) and vertical (bottom) profiles of family 2: 113.88—300.2 keV ARF tables in 83.97 – 102.63 keV energy window.

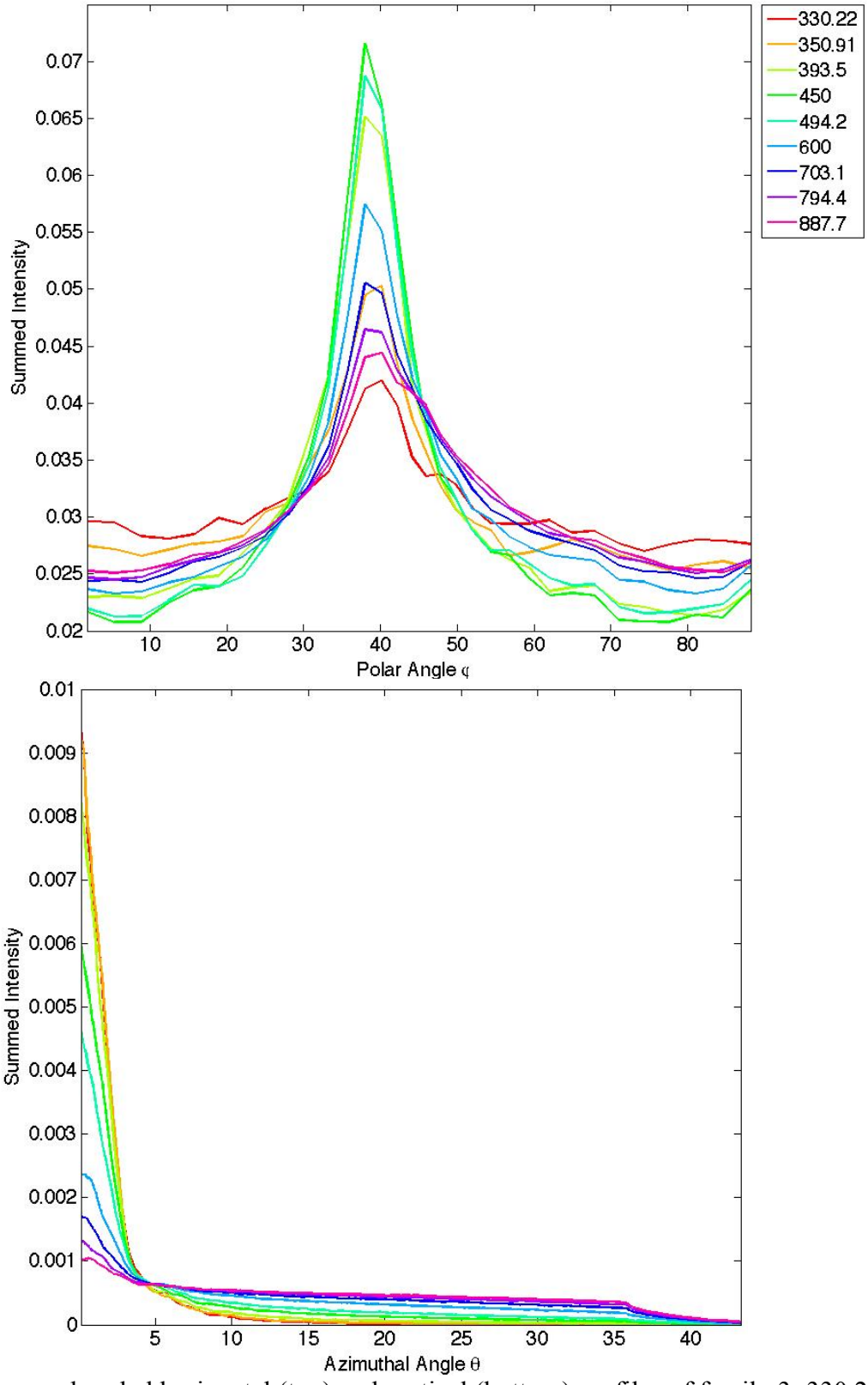

Figure 5.10. Summed scaled horizontal (top) and vertical (bottom) profiles of family 3: 330.22—887.7 keV ARF tables in 83.97 – 102.63 keV energy window.

Similarly, we divide the ARF tables in 166.14 – 203.06 keV energy window into three families: 147.68—213.54 keV, 240.16 keV—350.91 keV, and 393.5—887.7 keV. For 270.18 – 330.22 keV energy window the three families are: 240.16—330.22 keV, 337.10—494.2 keV, and 600—887.7 keV. Thus, it is very important to get the accurate ARF tables at the FWM points since they are the dividing points between the first and second families and will be used to estimate new ARF tables.

5.2 ^{67}Ga ARF Table Estimation

In order to use ARF tables in the MC simulations, we need to have ARF tables at every possible incident energy. Obviously this is not possible, because each 4 billion table requires up to 72 hours and each 100 million tables requires up to 1 hour to generate. We need methods for (1) determining at which energies tables are needed, (2) deciding how many photons should be simulated for each table, and (3) estimating tables at other energies are required. The existing literature is of little assistance here; for instance in Descourt et al. [27], a set of 44 ARF tables were computed in 10 keV wide energy intervals from 304 to 364 keV (6 intervals), 365 to 635 keV (27 intervals) and 639 to 709 keV (7 intervals). They stated that 5 billion up to 80 billion photons were simulated for each ARF table without saying how many photons for each table.
We propose the following algorithm to estimate new ARF tables:

1. Generate ARF tables with 4 billion decays at each of the ten emission energies of ^{67}Ga, the backscatter energies at which 180° backscatter will hit the energy window's top/bottom energy, the FWM energies around the peak.
2. Use ARF tables with 100 million decays in 10 keV intervals to get the accurate amplitudes of the energy points along the targeted energy range to minimize the gap between the tables.
3. Examine the amplitude curves from both the 4 billion and 100 million tables, and generate more 100 million tables at select energies in the sharp change regions on the amplitude curves to fill in the gaps so that we can get a smooth curve along the targeted energy range.

4. Assume A_2 is the normalized amplitude of the ARF table at energy E_2, E_1 and E_3 is the bracketing energies around E_2, and $E_1 < E_2 < E_3$. A_1 and A_3 are the normalized amplitude for E_1 and E_3 respectively. To estimate A_2:

$$A_2 = \frac{E_2 - E_1}{E_3 - E_1} \times A_3 + \frac{E_3 - E_2}{E_3 - E_1} \times A_1 \tag{5.2}$$

5. In order to estimate the ARF table f_2 at energy E_2:
   a. If $A_1 < A_2 < A_3$ or $A_3 < A_2 < A_1$,

$$f_2 = \left(\frac{A_2 - A_1}{A_3 - A_1} \times \frac{f_3}{A_3} + \frac{A_3 - A_2}{A_3 - A_1} \times \frac{f_1}{A_1}\right) \times A_2 \tag{5.3}$$

   b. Else if $|A_1 - A_2| < |A_3 - A_2|$,

$$f_2 = \frac{A_2}{A_1} \times f_1 \tag{5.4}$$

   c. Else,

$$f_2 = \frac{A_2}{A_3} \times f_3 \tag{5.5}$$

For example, to estimate the unknown ARF table for 410 keV in 83.97 – 102.63 keV energy window, we need to get the normalized amplitude for 410 keV and its bracketing energies from Figure 5.3. Because the percentage of normalized amplitude for 393.5 keV, 410 keV and 450 keV are: 5.48%, 6.89%, and 11.91%, we can use Equation (5.3) to get the estimated ARF table for 410 keV by interpolating from the ARF tables for 393.5 keV and 450 keV. Figure 5.11 shows the ARF tables for 393.5 keV and 450 keV used for interpolation on the top row, and the original versus interpolated ARF table for 410 keV on the second row. Note that because the 410 keV table is of low sensitivity, we used 40 billion decays to get the original ARF table to reduce the influence from noise. Figure 5.12 shows the summed scaled horizontal and vertical profiles of 393.5, 450, and the original and estimated 410 keV ARF tables in 83.97 – 102.63 keV energy window. We can see that the three adjacent tables represent similar characteristics in both the horizontal and vertical directions. We can make a comparison between the original and the interpolated 410 keV ARF tables by examining the summed horizontal and vertical profiles in Figure 5.12. The visual appearance of the curves for interpolated and the original ARF tables at 410 keV are similar in both directions. In the next section we quantify how good the agreement is.

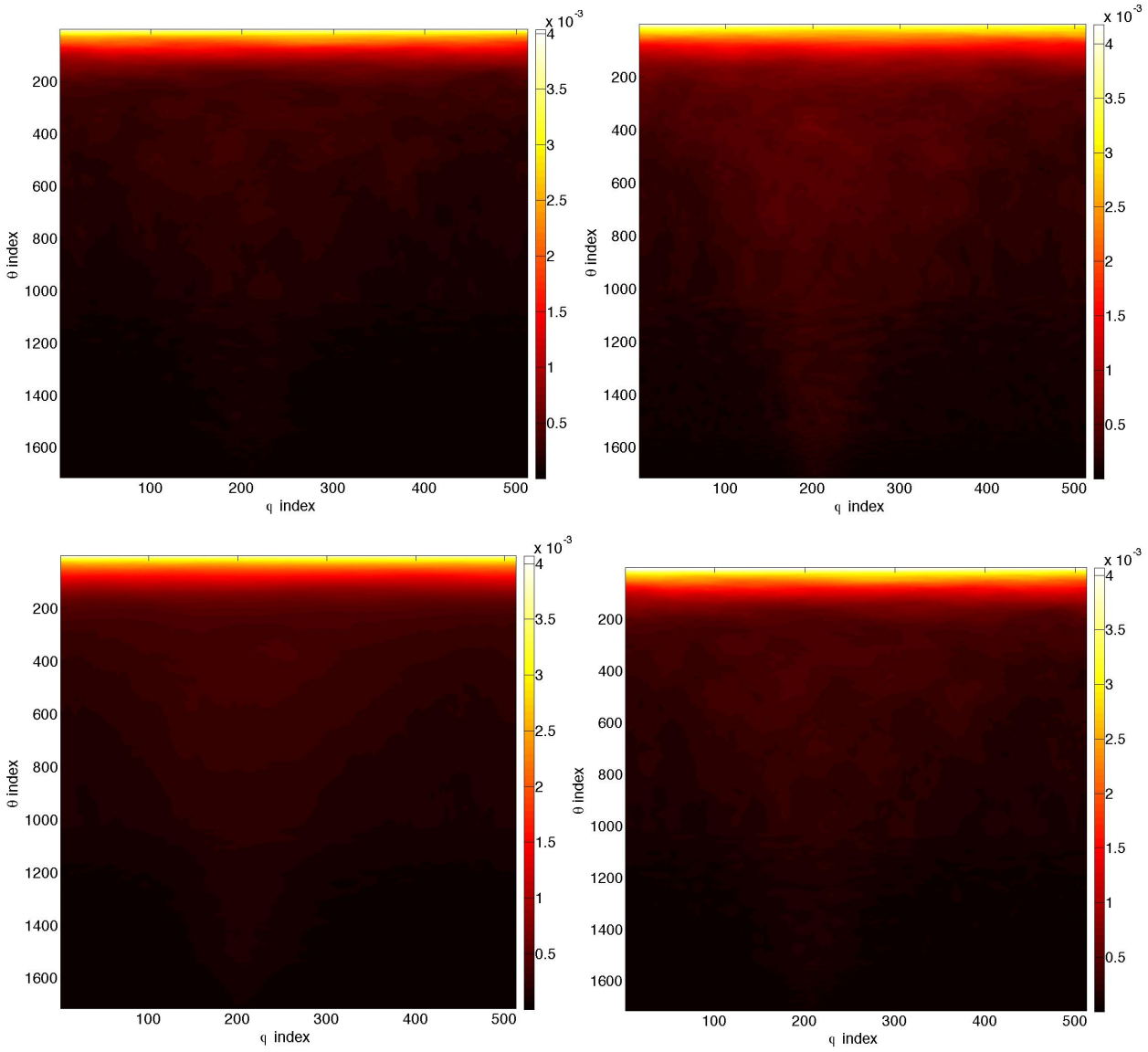

Figure 5.11. ARF tables for 393.5 keV (top left), 450 keV (top right), 410 keV (bottom left), and interpolated 410 keV (bottom right) in 83.97 – 102.63 keV energy window.

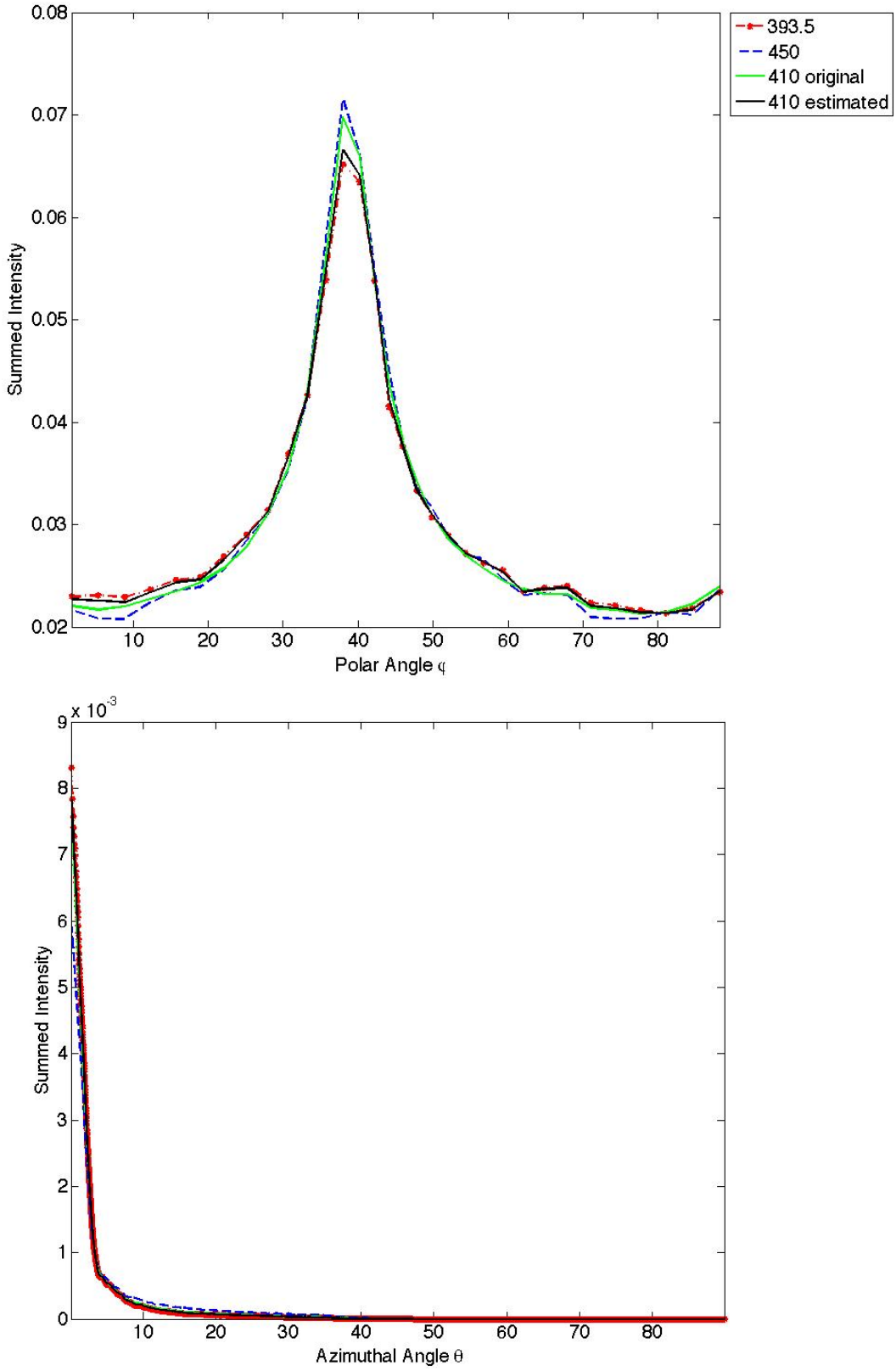

Figure 5.12. Summed scaled horizontal (top) and vertical (bottom) profiles of 393.5, 450, and the original and estimated 410 keV ARF tables in 83.97 – 102.63 keV energy window.

To estimate the ARF table for 184.6 keV in 83.97 – 102.63 keV energy window, we need to use Equation (5.4) or (5.5) to estimate the unknown ARF table. We get the normalized amplitude for 184.6 keV and its bracketing energies 164 keV and 194.35 keV from Figure 5.3: 1.70%, 1.95% and 1.83%. Therefore, we need to use the ARF table for 194.35 keV to estimate the ARF table for 184.6 keV using Equation (5.5).

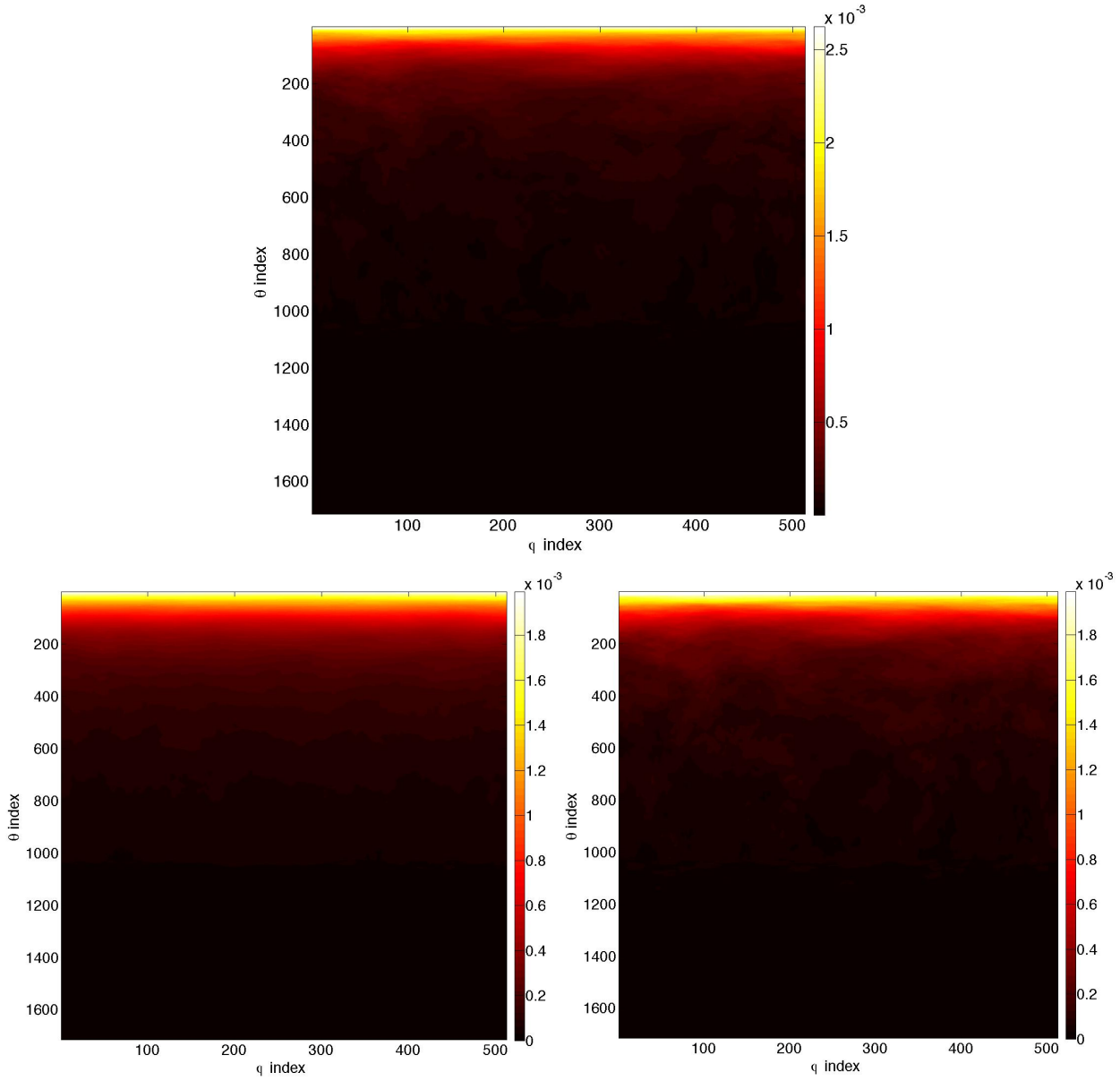

Figure 5.13. ARF tables for 194.35 keV (top), 184.6 keV (bottom left), and estimated 184.6 keV (bottom right) in 83.97 – 102.63 keV energy window.

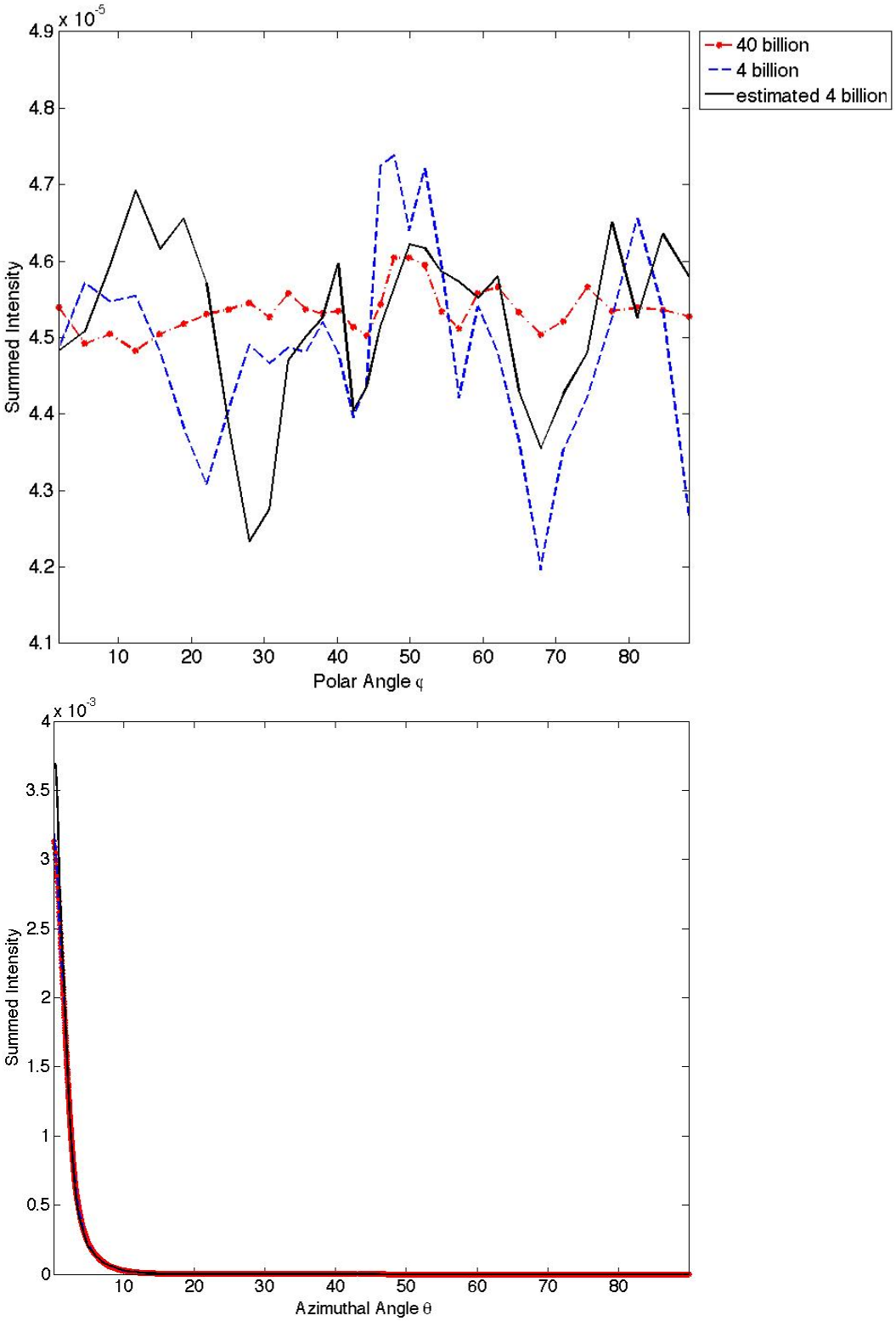

Figure 5.14. Summed horizontal (top) and vertical (bottom) profiles of the original 40-billion-decay, 4-billion-decay noisy and estimated 184.6 keV ARF tables in 83.97 – 102.63 keV energy window.

Figure 5.13 shows the ARF table for 194.35 keV used for estimation on the top row, and the original versus interpolated ARF table for 184.6 keV on the second row. Note that because the 184.6 keV table is of low sensitivity, we used 40 billion decays to get the original ARF table to reduce the influence from noise. We made a comparison between the original 40-billion-decay, 4-billion-decay noisy and the estimated 184.6 keV ARF tables by examining the summed horizontal and vertical profiles in Figure 5.14. The estimated table is very comparable to the characteristics of the original 4-billion-decay table in the horizontal. The three tables agree perfectly on the vertical direction.

To evaluate the accuracy of the ARF table estimation, we calculated both the root mean square error (RMSE) and the normalized root mean square error (NRMSE) between the original and the estimated ARF tables:

$$RMSE = \sqrt{\frac{\sum(p_1(\theta,\phi)-p_2(\theta,\phi))^2}{n}} \tag{5.6}$$

$$NRMSE = \frac{RMSE}{p_{max}-p_{min}} \tag{5.7}$$

where $p(\theta,\phi)$ is the probability for a specific bin at azimuthal angle θ and polar angle ϕ, and n is total number of bins in the ARF table.

In Table 5.2, we compared between the NRMSE of the estimated ARF tables versus the original ARF table simulated with 40 billion decays and the average NRMSE of 10 different 4-billion-decay ARF tables simulated using different random seed versus the original ARF table for selected energies in the three energy windows. With one exception, we find that comparisons of our estimated ARF tables to the original ARF tables gives NRMSEs in a range similar to those found between the original and generated with different random seeds. The comparison indicates that most of the estimated errors are within 1% of the maximum amplitude of the original table. Because they usually fall within 1 – 4 times the average of the NRMSE of the original versus 10 different 4-billion-decay tables, except the ARF table for 209 keV in energy window 166.14 – 203.06 keV. However, as seen in Figure 5.4, 209 keV falls near the transition region between the first family and the second family, and as it is in a low sensitivity region it is more likely to be influenced by noise. As 209 keV is one of the 10 emission energies for ^{67}Ga, we do use its table for our ARF-based simulations in any case: the estimated table is just used to show the limits of

our estimation algorithm's accuracy around a transition region. This is also the case for the table estimated for the 184.6 keV incident energy photons.

Table 5.2. Evaluation of ARF table estimation accuracy based on NRMSE comparison.

Energy Window (keV)	Point Source Energy (keV)	Bracketing Energy used for estimation (keV)	NRMSE of estimated versus original ARF tables	Average NRMSE of 10 different tables versus original table
83.97 – 102.63	184.6*	194.35	1.72E-02	9.50E-03
	410.0	393.5, 450	1.38E-02	6.70E-03
	650.0	600, 703.1	1.68E-02	1.38E-02
166.14 – 203.06	209.0*	203.06, 213.54	5.70E-03	6.03E-04
	410.0	393.5, 450	2.46E-02	5.90E-03
	650.0	600, 703.1	1.42E-02	8.30E-03
270.18 – 330.22	410.0	393.5, 430.52	1.83E-02	1.37E-02
	650.0	600, 703.1	1.14E-02	1.24E-02

*Note: These tables are shown to assess the estimation accuracy, but are not used for simulation purposes.

5.3 USE ARF TABLES IN SIMSET

We have implemented the ARF method as a user function in the SimSET software package to provide fast modeling of both interactions in the object and in the collimator-detector system. In the following example, we simulated a planar projection image of ^{68}Ge (511 keV) and ^{99m}Tc (140 keV) point sources in air and detected in the three energy windows for ^{67}Ga. To validate the results, we compared the simulated planar images, the sensitivity and the resolution to those derived from experimental data collected on our GE Discovery 670 SPECT System results using the same system and configurations. Due to conflicts in the information that we received from General Electric, we changed our simulation configuration to the: type (a) single-walled GE-Infinia-MEGP collimator, a 0.95 cm thick NaI crystal with 3.36 cm glass backscatter compartment behind, the energy resolution of 9.5% FWHM at 140 keV, a +/- 13% symmetric energy window around 93.3 keV and +/- 10% symmetric energy windows around 184.6 keV and 300.2 keV.

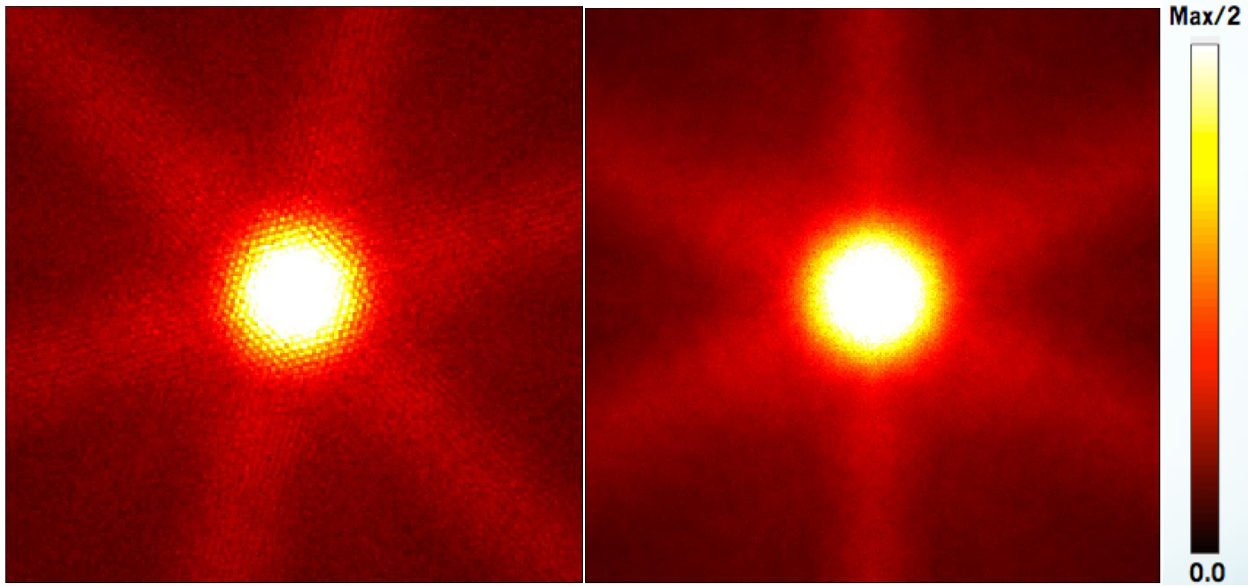

Figure 5.15. Planar images of a 511 keV point source in air for the GE Discovery 670 SPECT System (left) and the SimSET ARF simulation (right).

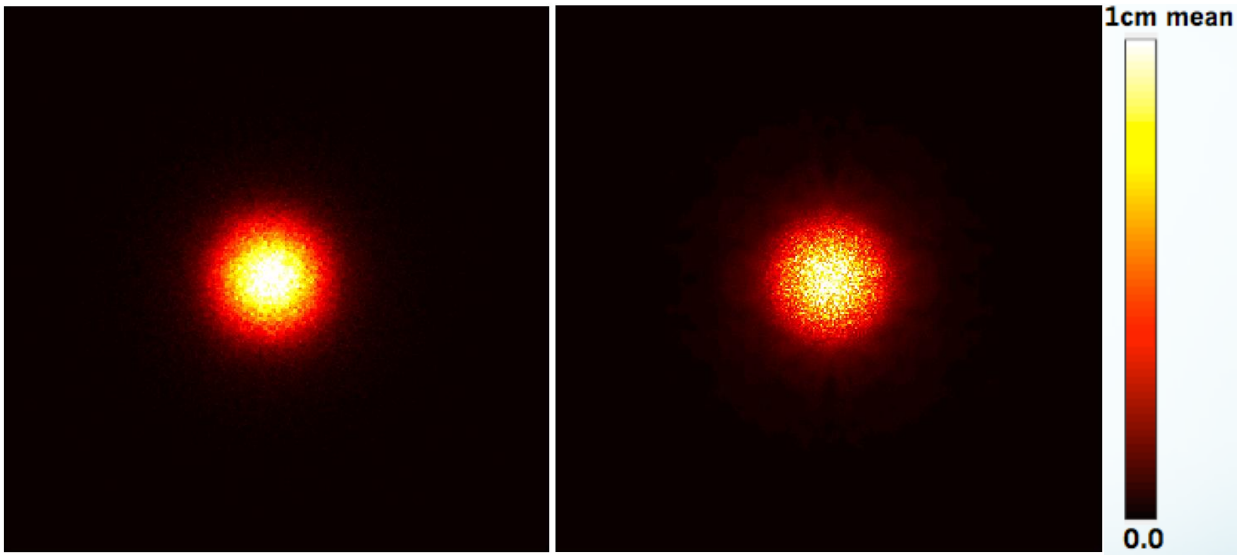

Figure 5.16. Planar images of a 140 keV point source in air for the GE Discovery 670 SPECT System (left) and the SimSET ARF simulation (right) normalized to the mean of the center 1cm radius region.

The comparison of the planar images between the experiment and simulation for ^{68}Ge and ^{99m}Tc point sources is shown in Figure 5.15 and Figure 5.16 respectively. There are two main differences from visual interpretation of the planar images of ^{68}Ge in Figure 5.15. First,

there is noticeable collimator hole pattern from the experiment image, while the simulated image is smoother. This is because the collimator hole pattern is removed from the raw ARF table, which has the collimator hole pattern, by averaging the sum of all the bins inside a disk with a fixed radius. Secondly, the experiment image is oriented diagonally by 15° due to the manufactured structure of the MEGP collimator holes' rows and columns orientation. There is a six-pointed star pattern of septal penetration in both the experiment image and simulated image. This confirms that the GE Discovery 670 SPECT System is a type (a) single-walled collimator instead of a type (b) double walled collimator as indicated in the information we received from General Electric previously. If we based our simulations on the assumption that the system has a double-walled collimator as shown in Figure 4.2 (b), our simulated image would present a four-pointed star pattern with only a faint increase in the axial directions. This is what one would expect if the septal walls were doubled in the axial direction. However, the image showing a six-pointed star pattern with equal intensity and separation is what one would expect if the septa were the same thickness in all six directions as shown in Figure 4.2 (a). The planar images of ^{99m}Tc between the experiment and simulation in Figure 5.16 showed similar characteristics. The simulation image is noisier as we collected 9.80E+10 photons during the experiment, but we only simulated 1.45E+9 photons in SimSET.

Table 5.3. Comparison between the clinical SPECT system and the SimSET ARF simulation.

Point Source	Experiment/Simulation	Sensitivity	FWHMx (mm)	FWHMy (mm)
^{68}Ge	Experiment	7.52E-05	76.26	75.01
	Simulation	5.89E-05	78.86	77.80
^{99m}Tc	Experiment	9.78E-06	64.71	64.24
	Simulation	2.27E-06	61.93	61.93

In Table 5.3, we compared the resolution as FWHM on the x and y axes between the experiment and simulated images. Looking at the sensitivity results, the sensitivity of the simulation is fairly close to the experiment for ^{68}Ge, but much lower than the experiment for ^{99m}Tc. The difference in sensitivity could because in the experimental setup the point sources were attached to one detector head while we collected data from the opposing detector head. The first detector head served as a backscatter compartment and therefore more photons were

detected within the energy window on the opposing detector head. Although we simulated the first detector head in SimSET, it is difficult to simulate an accurate geometry model for the first detector without detailed information of its covering material and the thickness. Because the 93.3 keV window is very sensitive to the 140 keV photons backscattered from the non-active head, only a few millimeter change in the thickness of the covering material will have a big influence on the simulation sensitivity. Moreover, there are other confounding factors such as scatter in the environment, which will result in more counts in the experiment. The resolutions of the planar images are very similar in the experiment and simulation results for both isotopes.

Chapter 6. CONCLUSION

In summary, we used the ARF method to examine the quantitative properties of ^{67}Ga SPECT imaging, developed a systematic method for ARF table estimation, and showed promising results by implementing an ARF feature in SimSET to provide accurate and efficient collimator-detector response modeling.

In Chapter 1, we briefly introduced the current research advances in Monte Carlo (MC) simulation for SPECT imaging. This motivates the study on modeling the collimator-detector response function (CDRF) to speed up the widely used but often time consuming MC simulations of SPECT. Therefore, in this thesis we focus on adding the Angular Response Function (ARF) feature to our public domain emission tomography simulation SimSET based on the method described by X. Song et al [9], and addressing some key challenges in the ARF table pre-calculation process.

In Chapter 2, we discussed the basic principles and components of a SPECT imaging system, and the imaging degradation factors in its performance, such as attenuation, collimator penetration, scattering and statistical noise. In Chapter 3, we introduced the MC simulation methods and its mathematical models. Various simulation software packages that are currently widely used in the medical imaging field are described and then used in the later chapters.

In Chapter 4, we first described an ARF parameterization method and how to generate ARF tables in SIMIND or GATE. Both methods are based on the GE Discovery 670 SPECT/CT system shown in Figure 2.2. We then presented a detailed ARF simulation for the ten ϒ ray emissions for ^{67}Ga to examine the imaging contamination. We choose ^{67}Ga because it is clinically used for tumor imaging, but the quantitative accuracy of the image is not well established and it is challenging to image. Significant contamination from collimator penetration and scatter was seen from simulation of point source in air for ^{67}Ga imaging. However, in patient imaging, there will be significant additional contamination from scatter in the patient and other confounding factors. Therefore, it is important to analyze and understand and improve quantification for ^{67}Ga imaging. Simulation is an ideal platform for this investigation, as factors such as scattered radiation, attenuation and partial volume can be separated and investigated independently. This can be achieved with the help from ARF simulations.

In Chapter 5, we first examined the characteristics of ^{67}Ga ARF tables generated by SPECT simulations within GATE. We then proposed our estimation algorithm to reduce the ARF pre-calculation requirements by using fewer tables and less photons to generate each table. The estimated tables are evaluated by comparing to the original low-noise ARF tables with more decays simulated, and the NRMSE are calculated to assess the estimation accuracy. Finally, the ARF tables are implemented as user functions in SimSET to simulate some planar images of a point source, and the results are compared based on the sensitivity and resolution. This comparison showed promising results. The SimSET-ARF simulation could greatly reduce the computation time of the traditional full MC collimator-detector tracking process, and provide an accurate collimator-detector response modeling at the same time.

We defined a method for using fewer tables and less photons to satisfy and standardize ARF pre-calculation requirements. We showed that the tables could be estimated reasonably well from the tables at nearby bracketing energies by comparing the estimated tables with original low noise tables generated with a large number of photons. The resulting tables can be used to do accurate simulation in SimSET and they matched with the experiment results using similar configurations. Our conclusions only apply to ^{67}Ga simulation using MEGP collimators. However, the conclusions for ^{67}Ga should be generalizable to most commonly used Nuclear Medicine isotopes because (1) the range of ^{67}Ga emitted photon energies covers the range of emission energies for most isotopes and (2) the three energy windows are close to the energy windows used for many of the clinically used isotopes. Using the SimSET-ARF method, it is now practical to simulate low noise SPECT projection data in reasonable computation times, especially in cases where collimator-detector interactions are important and in simulation-based evaluations of compensation methods involving large number of phantoms.

BIBLIOGRAPHY

[1] Phelps, Michael E. Physics in nuclear medicine. Diss. University of Wisconsin-Madison, 1987.

[2] Anger, Hal O. "Scintillation camera." Review of scientific instruments 29.1 (1958): 27-33.

[3] Harrison, Robert L. "Simulation of medical imaging systems: emission and transmission tomography." Handbook of Particle Detection and Imaging. Springer Berlin Heidelberg, 2012. 1095-1124.

[4] Wang, Wen-Tung, et al. "Optimization of acquisition parameters for simultaneous 201 Tl and 99m Tc dual-isotope myocardial imaging." Nuclear Science, IEEE Transactions on 52.5 (2005): 1227-1235.

[5] Wang, W. T., et al. "A model-based crosstalk compensation method for simultaneous Tl-201 And Tc-99m dual isotope myocardial SPECT imaging."Nuclear Science Symposium Conference Record, 2001 IEEE. Vol. 4. IEEE, 2001.

[6] Du, Y., et al. "Combination of MCNP and SimSET for Monte Carlo simulation of SPECT with medium-and high-energy photons." Nuclear Science, IEEE Transactions on 49.3 (2002): 668-674.

[7] De Jong, Hugo WAM, et al. "Efficient simulation of SPECT down-scatter including photon interactions with crystal and lead." Medical physics 29.4 (2002): 550-560.

[8] Dewaraja, Yuni K., Michael Ljungberg, and Kenneth F. Koral. "Monte Carlo evaluation of object shape effects in iodine-131 SPET tumor activity quantification." European journal of nuclear medicine 28.7 (2001): 900-906.

[9] Song, X., et al. "Fast modelling of the collimator–detector response in Monte Carlo simulation of SPECT imaging using the angular response function."Physics in medicine and biology 50.8 (2005): 1791.

[10] Crespo, Cristina, et al. "Quantification of dopaminergic neurotransmission SPECT studies with 123I-labelled radioligands. A comparison between different imaging systems and data acquisition protocols using Monte Carlo simulation."European journal of nuclear medicine and molecular imaging 35.7 (2008): 1334-1342.

[11] Cot Sanz, Albert. "Absolute quantification in brain SPECT imaging." (2003).

[12] Metz, Charles E., F. B. Atkins, and Robert N. Beck. "The geometric transfer function component for scintillation camera collimators with straight parallel holes." Physics in medicine and biology 25.6 (1980): 1059.

[13] Tsui, B. M. W., and G. T. Gullberg. "The geometric transfer function for cone and fan beam collimators." Physics in medicine and biology 35.1 (1990): 81.

[14] Frey, E. C., B. M. W. Tsui, and G. T. Gullberg. "Improved estimation of the detector response function for converging beam collimators." Physics in medicine and biology 43.4 (1998): 941.

[15] Formiconi, Andreas Robert. "Geometrical response of multihole collimators."Physics in medicine and biology 43.11 (1998): 3359.

[16] Cot, A., et al. "Evaluation of the geometric, scatter, and septal penetration components in fan-beam collimators using Monte Carlo simulation." Nuclear Science, IEEE Transactions on 49.1 (2002): 12-16.

[17] Moore, Stephen C., Marie Foley Kijewski, and G. El Fakhri. "Collimator optimization for detection and quantitation tasks: application to gallium-67 imaging." Medical Imaging, IEEE Transactions on 24.10 (2005): 1347-1356.

[18] Ljungberg, Michael, Sven-Erik Strand, and Michael King. "Monte Carlo Calculation in Nuclear Medicine: Applications in Diagnostic Imaging." (1998).

[19] Jan, S., et al. "GATE: a simulation toolkit for PET and SPECT." Physics in medicine and biology 49.19 (2004): 4543.

[20] Song, X., et al. "Fast modelling of the collimator–detector response in Monte Carlo simulation of SPECT imaging using the angular response function."Physics in medicine and biology 50.8 (2005): 1791.

[21] Harrison, Robert L., and Tom K. Lewellen. "The SimSET Program." Monte Carlo Calculations in Nuclear Medicine: Applications in Diagnostic Imaging(2012): 87.

[22] Ljungberg, Michael. "The SIMIND Monte Carlo program." Monte Carlo calculations in nuclear medicine: Applications in diagnostic imaging (2012): 111- 28.

[23] Moore, Stephen C., Marie Foley Kijewski, and G. El Fakhri. "Collimator optimization for detection and quantitation tasks: application to gallium-67 imaging." Medical Imaging, IEEE Transactions on 24.10 (2005): 1347-1356.

[24] Palestro, Christopher J. "The current role of gallium imaging in infection."Seminars in nuclear medicine. Vol. 24. No. 2. WB Saunders, 1994.

[25] Mansberg, Robert, Surjit S. Wadhwa, and Victor Mansberg. "Tl-201 and Ga-67 scintigraphy in non-Hodgkin's lymphoma." Clinical nuclear medicine 24.4 (1999): 239-242.

[26] Tuli, Mahmoud M., et al. "The use of gallium-67 scintigraphy to monitor tumor response rates and predict long-term clinical outcome in patients with lymphoma." Clinical lymphoma 5.1 (2004): 56-61.

[27] Descourt, Patrice, et al. "Implementation of angular response function modeling in SPECT simulations with GATE." Physics in medicine and biology55.9 (2010): N253.